PEOPLES DEMOCRATIC REPUBLIC OF ALGERIA

MINISTRY OF HIGHER EDUCATION AND SCIENTIFIC RESEARCH

UNIVERSITY OF MOHAMED BOUDIAF - M'SILA

FACULTY OF SCIENCES

DEPARTMENT OF PHYSICS

N° : PH/ENR/05/2025

FIELD: MATERIAL SCIENCES

FIELD: PHYSICS

OPTION: PHYSICS OF ENERGY AND RENEWABLE ENERGIES

Memory Submitted for Obtaining

Diploma of Academic Master

Submitted by:

BENCHABANE Ahlam **TAIBAOUI Ferial**

Entitled

Investigation of the electronic and optical properties of the compound Ba_2BBiO_6 (B = Sm, Tb) double perovskite oxides and their potential applications in photovoltaic cells

Defended on 22/06/2025 in front of a jury composed of:

Djelel Kherifi	University Mohamed Boudiaf- M'sila	Chairperson
Karim Bouferrache	University Mohamed Boudiaf- M'sila	Supervisor
Saber Saadessaoud	University Mohamed Boudiaf- M'sila	Examinator

Academic Year: 2024/2025

Thanks

We would like to express our deepest gratitude and sincere appreciation to our esteemed supervisor

"Dr. Bouferrache Karim"

for his insightful guidance, continuous support, and great patience throughout all stages of this work. His scientific rigor, valuable advice, and respectful mentorship have greatly contributed to the success and quality of our research.

We also extend our heartfelt thanks and appreciation to the respected members of the examination committee:

Professor Djelel Kherifi

*and **Professor Saber Saadessaoud**,*

for their precious time, constructive remarks, and valuable suggestions that greatly contributed to enriching and improving this research.

Dedication I

To the ones who have always been a source of inspiration and strength,

To my beloved parents

Thank you for your unconditional love, your unwavering support, and your constant belief in me.

You have been the foundation upon which all my efforts were built, and the steadfast pillars that held me up through every challenge.

And to my dear friends:

AMINA, IKRAM, AMIRA** and **DOUNIA

Thank you from the bottom of my heart for your genuine friendship, your comforting presence, and your encouraging words that always pushed me forward.

You have been the chosen family, the companions in both the journey of learning and the moments in between. Your support has truly been a blessing.

I dedicate this humble word to all of you – in gratitude appreciation, and lasting affection.

AHLAM

Dedication II

To the ones who gave me life and stood by my
side through every step

To my beloved parents

Thank you for your unconditional love,
countless sacrifices, and unwavering faith in me,
even during the times when I doubted myself.

You have been the light that guided my path and
the refuge I always return to.

And to my small, cherished family

My constant source of warmth and comfort,

I dedicate this work to you, as a token of
deep gratitude and lasting devotion.

This achievement is yours as much as it is
mine.

FERIAL

Table of Contents

INTRODUCTION 11

CHAPTER 1……………………………………………………………………..15

I.1 Introduction………………………………………………………….…….…...16

I.2 Perovskite structure…………………………………………………..……..16

I.2.1 Ideal perovskite structure……………………………………………..16

I.2.2 Description of perovskite structure……………………………….…...17

I.2.3 Classification of Perovskite Structures…………………………18

I.3 Structural Stability Conditions of Perovskite…………………………..18

I.3.1 Tolerance Factor (T)……………………………………………..19

I.3.2 Ionic Character of Anion-Cation Bonds…………………………20

I.4 Perovskite distortions……………………………………………………21

I.4.1 The Jahn-Teller effect………………………………………………...21

I.4.2 Glazer Notation for Octahedral Tilts……………………………22

I.5 Families of perovskite…………………………………………………....23

I.6 Types of perovskites……………………………………………………...24

I.6.1 Tetragonal perovskite…………………………………………….....24

I.6.2 Rhombohedral Perovskite………………………………………24

I.6.3 Orthorhombic Perovskite………………………………………..24

I.7 Crystalline structure of double perovskite……………………………..25

I.8 Stability of the Double Perovskite Structure…………………………...25

I.9 Electronic properties of double perovskites……………………………26

I.10 Property of half-metallicity…………………………………………......26

I.11 Magnetic properties of double perovskites……………………………..27

I.11.1 Diamagnetism……………………………………………...28

I.11.2 Paramagnetism……………………………………………..28

I.11.3 Antiferromagnetism………………………………………..29

I.11.4 Ferromagnetism………………………………………………30

I.11.5 Ferrimagnetism………………………………………………32

I.12 Perovskite Materials: Their Uses and Applications…………………...32

I.12.1 Fuel Cells Made of Solid Oxide (SOFC)………………………32

I.12.2 Photovoltaic Devices…………………………………………33

I.12.3 Devices by Spintronics…………………………………………33

I.13 Conclusion……………………………………………………………..33

CHAPTER 2……………….……………………………………………………37

II.1 Introduction……………………………………………………………...38

II.2 The Schrödinger equation of a crystalline solid……………………….38

II.3 The Born-Oppenheimer Approximation………………………………39

II.4 The-Hartree-Fockapproximation………………………………………40

II.5 The Density Functional Theory (DFT)………………………………...41

II.5.1 Origin of the DFT………………………………………………...41

II.5.2 The Thomas-Fermi approximation…………………………… 42

II.5.3 The Hohenberg-Kohn theorem…………………………..…… 43

II.5.4 First theorem of Hohenberg and Kohn…………………….. 43

II.5.5 Second theorem of Hohenberg and Kohn…………………… 43

CHAPTER 3…….…………………………………………………..………53

III.1 Introduction………………………………………………………...………54

III.2 Crystal structure...54

III.3 The structural properties of the compound..56

III.4 Energy Band Structure...60

III.5 Electronic Density of States (DOS)………………………………………..64

III.6 Optical properties……………...…………………………………..64

III.6.1 Dielectric Function ε(ω)…………………………..………...71

III.6.2 Refractive Index……………………………………………...71

III.6.3 The Extinction Coefficient………………………………...73

III.6.4 Absorption Coefficient: α(ω)……………………………...74

III.6.5 The energy loss function (L(ω))………………………………..76

III.6.6 Optical Conductivity σ(ω)……………………………...77

III.7 Conclusion………………………………………………………..79

GENERAL CONCLUSION ………………………………………………... 82

ABSTRACT……………………………………………………………………84

List of figures

Figures	Titles	Pages
Figure (I.1)	Cubic perovskite unit cell, blue spheres represent the A cations, yellow sphers for B cation, and red for oxygen anions forming an octahedral	16
Figure. I.2	Representations of the perovskite structure	17
Figure I.3	Periodic table of atoms that can be accommodated on the A and B sites of the perovskite lattice.	18
Figure I.4	Effect of the Tolerance Factor on Crystal Structure and Atomic Arrangement.	20
Figure. I.5	A schematic diagram indicating the group- subgroup relationships among the 15 space groups tabulated by Howard & Stokes (1998).	23
Figure. I.6	Structural representation of a double perovskite $A_2BB'X_6$	25
Figure. I.7	. **(a)** Variations of magnetization in response to a magnetic field. (b) Thermal variation of magnetic susceptibility	28
Figure. I.8	Paramagnetism of Isolated Atoms.	29
Figure. I.9	Antiferromagnetism: (a) spin lattice; (b) M=f(H); (c) 1/X ~(T)	30
Figure. I.10	Ferromagnetism: (a) Spin lattice; (b) Magnetization variation under an external field (Tj < Tc < T2 < T3); (c) Thermal variation of (1/X); (d) Thermal variation of spontaneous magnetization	31
Figure. I.11	Magnetization curve of an unmagnetized material or initial magnetization curve (solid line) - Hysteresis loop (dashed lines)	31
Figure. I.12	Ferrimagnetism: (a) Spin lattice; (b) Thermal variation of 1/x; (d) Thermal variation of spontaneous magnetization; (c) Variation of magnetization under a magnetic field	31
Figure. II.1	Self-consistent iterative process used to solve the Kohn-Sham equations.	46

Figure. III.1	Schematic crystal structure of Ba_2BBiO_6 (B= Sm, Tb)	55
Figure. III.2	The calculated energy vs. volume curves for optimizing of Ba_2BBiO_6 (B= Sm, Tb) using GGA approximation for Magnetic and non-magnetic phases	58
Figure. III.3	The first Brillouin zone of FCC structures	60
Figure. III.4	The band structures for spin (up) and spin (dn) configuration of Ba_2SmBiO_6 (a) using GGA (b) with mBJ-GGA	61
Figure. III.5	Density of states for spin (up) and spin (dn) configuration of (a) Ba_2SmBiO_6 (b) Ba_2TbBiO_6 using mBJ-GGA	63
Figure III.6	Partial density of states pdos for spin (up) and spin (dn) configuration of (a) Ba_2SmBiO_6 (b) Ba_2TbBiO_6 using mBJ-GGA	65
Figure III.7	Density of states for spin (up) and spin (dn) configuration of (a) Ba_2SmBiO_6 (b) Ba_2TbBiO_6 using mBJ-GGA	68
Figure III.8	Imaginary part of the dielectric function (ε_2) as a function of energy for Ba_2SmBiO_6 and Ba_2TbBiO_6	69
FigureIII.9	Real part of the dielectric function analysis for Ba_2SmBiO_6 and Ba_2TbBiO_6 compounds	70
Figure. III.10	The variations of the real part of the refractive index with photon energy for Ba_2SmBiO_6 and Ba_2TbBiO_6	72
Figure. III.11	. Variation of the extinction coefficient with photon energy for Ba_2SmBiO_6 and Ba_2TbBiO_6 compounds	74
Figure. III.12	The absorption coefficients of the compound Ba_2BBiO_6 using the GGA approximation	75
Figure III.13	The energy loss function for Ba_2BBiO_6 (B= Sm, Tb) perovskites utilising mBJ-GGA	76
Figure III.14	Optical conductivity curve ($\sigma(\omega)$) for both compounds, Ba_2SmBiO_6 and Ba_2TbBiO_6	77

List of tables

Tables	Titles	Pages
Table I.1	Expected Crystallographic Structures Based on the Value of the Goldschmidt factor	19
Table III.2	the calculated structural parameters of Ba_2SmBiO_6 and Ba_2TbBiO_6 in both non magnetic (NM) and ferromagnetic (FM) states	59
Table III.3	The band gap of Ba_2BBiO_6 (B=Sm, Tb) using GGA, and mBJ	62
Table III.4	Comparison Between Ba_2SmBiO_6 and Ba_2TbBiO_6	78

INTRODUCTION

One of the most important challenges facing our society today is to look for clean and renewable energy sources in order to mitigate the rapidly increasing energy demand for the growing population and industrialization that's why Perovskite materials have become one of the most prominent research areas in renewable energy and advanced materials over the past few decades [1]. These materials are characterized by their unique crystalline structure, resembling the natural perovskite mineral ($CaTiO_3$) [2], which can vary depending on their constituent elements. This diversity grants them unique properties such as thermal stability, electronic efficiency, and excellent optical characteristics, making them strong candidates for applications in solar energy technologies, especially high-efficiency solar cells.

In recent years, increasing attention has been directed toward the study of double perovskite materials due to their promising potential in various applications, including solar cells, electronic devices, and magnetics. Double perovskite compounds feature a more complex and versatile crystalline structure, allowing precise tuning of electronic and optical properties through the selection of suitable elements [3].

This thesis aims to study the structural, electronic, and optical properties of two double perovskite compounds of the type Ba_2BBiO_6, where B = Sm, Tb. This objective will be achieved by employing Density Functional Theory (DFT) as the main tool to simulate the various properties of these compounds. Additionally, the simulated results will be analyzed to understand the relationship between the crystal structure, electronic properties, and the potential applications of these compounds, particularly in the field of solar cells.

The thesis is organized into three main chapters, each focusing on different aspects of the topic:

Chapter 1: General Overview of Perovskite Materials

- Definition and Crystal Structure: Provides a general definition of perovskite materials, focusing on the basic crystal structure (ABX_3) and its variants [4].
- Key Properties: Reviews the electronic, optical, and thermal properties of perovskite materials, emphasizing their practical applications such as solar cells.
- Double Perovskite Compounds: Explains the unique crystal structure of double perovskite compounds and the role of different elements in determining their properties.

Chapter 2: Density Functional Theory (DFT)

- Introduction to DFT: Offers an overview of Density Functional Theory as a computational tool for studying the electronic properties of materials.

- Fundamentals of the Theory: Explains the theoretical foundations, including the Hartree-Fock principle and the density functional approximation.
- Computational Tools: Describes the computational tools used in simulations, and how they are applied to study electronic and structural properties.

Chapter 3: Simulation Results and Analysis of Structural, Electronic, and Optical Properties

- Structural Results: Analyzes the crystal structure results of Ba_2SmBiO_6 and Ba_2TbBiO_6 using DFT.
- Electronic Properties: Studies the electronic properties, such as energy levels, band gap, and charge behavior within the compounds.
- Optical Properties: Evaluates the optical properties, including refractive index, light absorption, and the compounds' interaction with light radiation.
- Potential Applications: Draws conclusions about the feasibility of using these compounds in solar cells or other applications based on the obtained results.

This study holds significant importance in the context of scientific research and practical applications. Understanding the electronic and optical properties of double perovskite materials helps in designing new materials with higher efficiency in the field of renewable energy, particularly solar cells. Furthermore, the results of this study can contribute to improving our understanding of the relationship between crystal structure and the physical properties of materials, opening new avenues for innovation in advanced materials.

- Crystal Structure Analysis: Study the crystal structure of Ba_2SmBiO_6 and Ba_2TbBiO_6 using DFT.
- Evaluation of Electronic Properties: Analyze energy levels, band gap, and charge behavior within the compounds.
- Analysis of Optical Properties: Examine how the compounds interact with light radiation and assess the refractive index.
- Application Conclusions: Provide conclusions regarding the potential use of the compounds in solar cells or other applications.

The study will primarily rely on atomic and chemical computational tools using Density Functional Theory. Various properties of the compounds will be simulated using advanced computational software, with a scientific and precise analysis of the results. Additionally, the simulated results will be compared with available experimental data from the scientific literature, if available.

This thesis focuses specifically on two double perovskite compounds, Ba_2SmBiO_6 and Ba_2TbBiO_6. While the study provides detailed insights into their structural, electronic, and optical properties, it does not cover synthesis or experimental characterization, as the research is based purely on computational simulations. Furthermore, while comparisons to experimental data will be drawn when possible, the predictive nature of DFT inherently carries certain approximations and assumptions, which will be acknowledged and discussed.

This study seeks to provide an integrated scientific contribution to understanding the structural, electronic, and optical properties of two double perovskite compounds. By employing GGA and mBJ as a primary tool, the study will highlight the relationship between crystal structure and the physical properties of materials, enhancing our understanding and opening new doors for future applications in renewable energy and advanced materials.

References:

[1] Tomar, P., Oosterbaan, S., Sharma, G., Yan, Q., & Mola, G. T. (2020). Perovskites photovoltaic solar cells: An overview of current status. Renewable and Sustainable Energy Reviews, 134, 110328.

[2] J. Paul Attfield,a Philip Lightfootb and Russell E. Morrisb , (2015). " Perovskites".| Dalton Trans., 44,10541–10542.

[3] Jafar, Aqel Mashot, et al. (2020). "Lead-free perovskite and double perovskite solar cells." *IOP Conference Series: Materials Science and Engineering*, Vol. 765, No. 1, pp. 012047

[4] Hazen, Robert M. (1988). "Perovskites." *Scientific American*, Vol. 258, No. 6 (JUNE),
pp. 74-81. Published by Scientific American, a division of Nature America, Inc.

Chapter *1: General Overview of Perovskite Materials*

I.1 Introduction

Perovskites are a family of materials that have shown great attention due to their high performance and low production costs in solar cells. The name "Perovskite" comes from the Russian geologist *Lev Perovski. Perovskite*, compounds adopt the general formula ABX_3, where A and B are cations with various atomic radii (A is larger than B), and X is an anion. The crystal structure of organic-inorganic hybrid metal halide perovskites shares the same type with the calcium titanium oxide ($CaTiO_3$), a mineral that was first discovered.

These materials are extensively studied for their applications in solar cells, led and other energy applications.

I.2 Perovskite structure

I.2.1 Ideal perovskite structure

The ideal perovskite structure is a cubic structure and follows the chemical formula ABX_3. However, only a few perovskite compounds have this perfect cubic structure. The cubic stacking is constructed with three types of atoms: A, B and X where **(Fig.1.1)**: [1]

- A is a cation with a large ionic radius (Ba, Ca, Pb, Rb, Sr, Na, K...).
- B is a cation with a smaller ionic radius (Ti, Sn, W, Zr, Nb, Ta...).
- X is an anion that can be an oxide or fluoride, and in some cases, Chloride or Bromide [2].

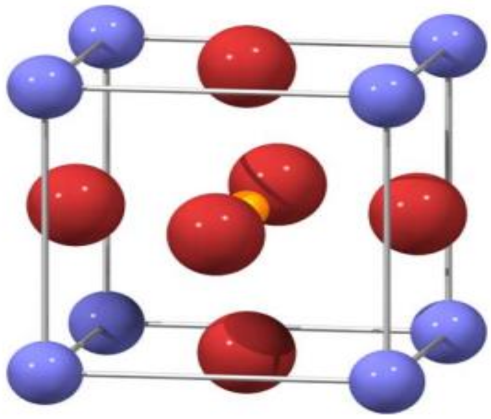

Figure 1.1. Cubic perovskite unit cell, blue spheres represent the A cations, yellow sphers for B cation, and red for oxygen anions forming an octahedral.

I.2.2 Description of perovskite structure

The structural representation of perovskite can be described by positioning the origin at one of the two cations, A or B, following the Miller and Love notation [3].

In the first representation, **(Fig.1. 2.a)**, A is placed at the origin, at position 1a (0, 0, 0), while B is situated at the cube's center, at position (½, ½, ½). The anions (such as oxygen) are located at the center of each face, in position 3c (0, ½, ½).

In the second representation, **(Fig.1.2.b)**, the origin is shifted by a vector (½, ½, ½), placing A at position 1b (½, ½, ½), B at position 1a (0, 0, 0), and the anions at the midpoint of each edge, at position 3d (0, 0, ½).

The structure is typically made up of a three-dimensional network of BO6 octahedra, with site B having a coordination number of 6 **(Fig.1.2.c)**, connected at their vertices. The spaces between these octahedra form cuboctahedra, with the center of these cuboctahedra representing site A, which has a coordination number of 12 **(Fig.1.2.d)** [4].

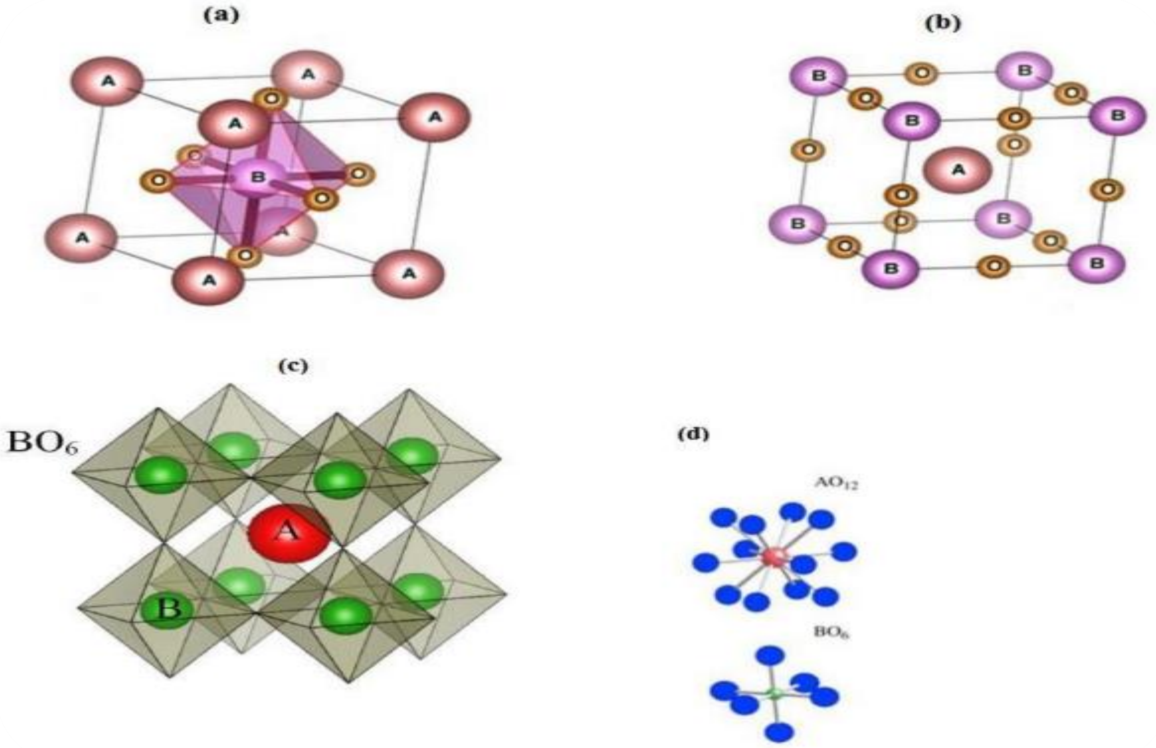

Figure 1.2. Representations of the perovskite structure: (a) The unit cell with A at the origin, (b) B at the origin, (c) The three-dimensional network of [BO_6] octahedral, and (d) Representation of the environment around the A and B sites.

I.2.3 Classification of Perovskite Structures

Perovskite structures are categorized based on the elements occupying the A and B sites. According to this classification, they are divided into two main types **(Fig.1.3)**:

- **Simple Perovskite Structures:** In this type, the A and B cations occupy a single type of atomic site. Examples include: $BaTiO_3$, $PbTiO_3$, $CaTiO_3$, etc.
- **Complex Perovskite Structures:** Here, the A and B sites are partially occupied by two different types of cations, leading to a mixed composition. Examples include: $PbSc_1/_2Ta_1/_2O_3$, $Na_1/_2Bi_1/_2TiO_3$, etc. [5].

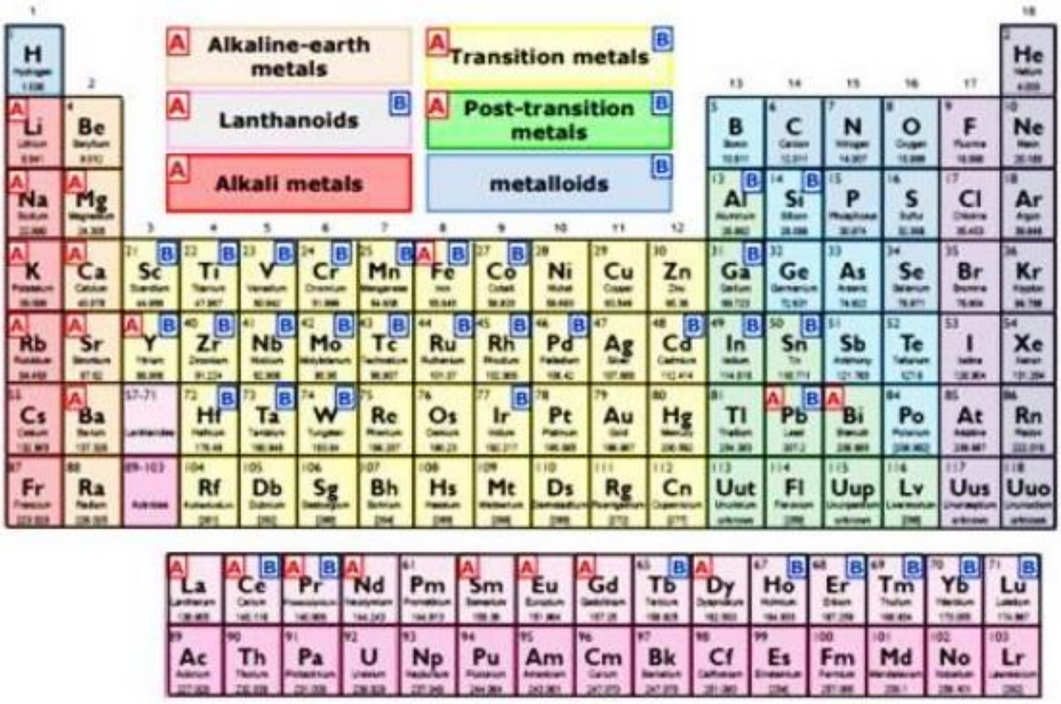

Figure 1.3. Periodic table of atoms that can be accommodated on the A and B sites of the perovskite lattice.

I.3 Structural Stability Conditions of Perovskite

The stability of perovskite structures is influenced by several key factors, with the tolerance factor being one of the most significant. Additionally, Glazer’s classification is commonly used to describe structural distortions, except under extremely high-pressure conditions.

I.3.1 Tolerance Factor (T)

The tolerance factor is a numerical value introduced by V.M. Goldschmidt in 1927. It serves as an indicator of the degree of structural distortion in perovskite materials. This factor is determined by the ionic radii of the elements involved and is used to assess the geometric compatibility between the AX and BX_3 bonds. If the ionic radii are within an optimal range, the perovskite structure remains stable. However, if the radii deviate significantly, structural distortions may occur, potentially altering the material's symmetry and phase.

The Goldschmidt tolerance factor (t) is an important empirical index for predicting the stable crystal structures of perovskite materials. (t) defined as follows:

$$\boldsymbol{t} = \frac{\boldsymbol{r_a} + \boldsymbol{r_x}}{\sqrt{2}(\boldsymbol{r_b} + \boldsymbol{r_x})}$$

Where r_a and r_b are the ionic radii of the A and B site cations, respectively, and r_x is the ionic radius of the anion.

Experimentally, the perovskite structure is considered stable for: $0.71 \leq t \leq 1.06$. This range, therefore, allows for variations in compositions, particularly in terms of the cations used [6].

Table I.1. Expected Crystallographic Structures Based on the Value of the Goldschmidt Factor.

Value of t	Possible structure(s)	Explanation
>1	Hexagonal	The size of the cation A is too large for A to occupy the cuboctahedral site
From 0.9 to 1	Cubic	The size of the ions is ideal
From 0.71 to 0.9	Orthorhombic, rhombohedral	The size of the cation A is too small to fully occupy the cuboctahedral site
< 0.7	Other structures	The size of cation A is similar to that of cation B.

The structural configuration of a material can change depending on the tolerance factor (*t*) when compared to an ideal cubic structure:

- **For t > 1,** instability is primarily associated with B sites. In this case, the A cation occupies the cuboctahedral cavity, while the B cation is smaller than the octahedral site it resides in. As a result, the B cation shifts within its cavity to shorten certain B-O bonds and reduce its coordination number. This phenomenon often favors the emergence of a polar and ferroelectric structure, which is observed in materials such as $BaTiO_3$ and $PbTiO_3$.
- **For t < 1,** instability is mainly influenced by A sites. Here, the B cation fills the octahedral cavity, whereas the A cation is smaller than the available cuboctahedral cavity. This can lead to a rotation of octahedra, which helps to minimize A-O distances. Additionally, the A cation may shift away from the center of its cavity. This behavior is evident in $BiFeO_3$, where both octahedral rotation and simultaneous displacement of A and B cations are observed [6].

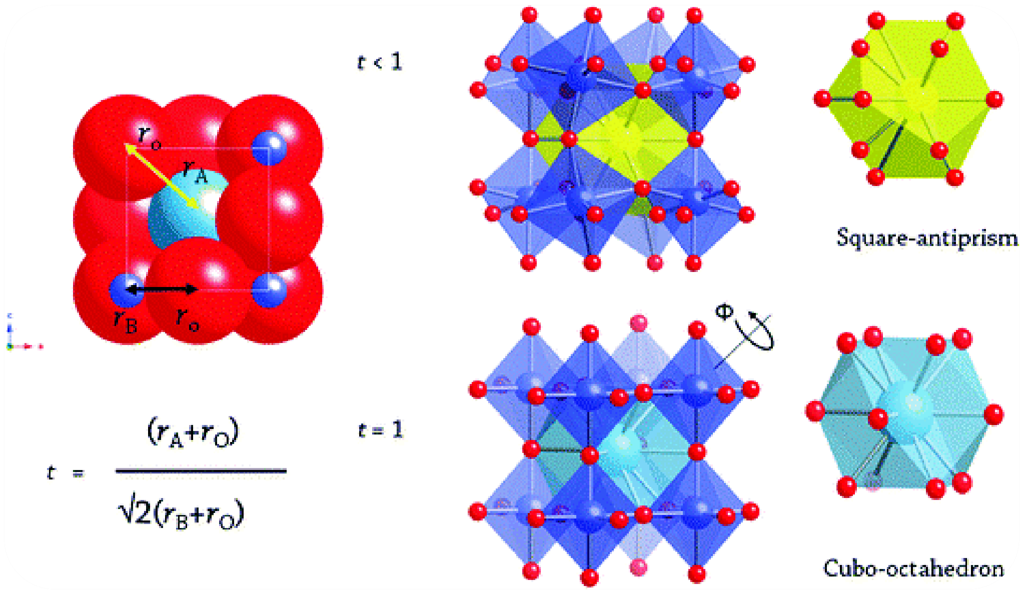

Figure 1.4. Effect of the Tolerance Factor on Crystal Structure and Atomic Arrangement.

I.3.2 Ionic Character of Anion-Cation Bonds

The difference in electronegativity between the ions in an ABO_3 perovskite structure serves as an indicator of its stability. A perovskite structure tends to be more stable when the bonds between cations and anions exhibit a high degree of ionic character. The ionic nature of these bonds can be estimated using the following equation: [7]

$$\bar{X} = \frac{(X_A - X_B\ ) + (X_B - X_O)}{2}$$

Where (X_A-X_B) and (X_B-X_O) represent the electronegativity differences between element A and oxygen, and element B and oxygen, respectively.

I.4 Perovskite distortions

I.4.1 The Jahn-Teller effect

The Jahn-Teller effect (JTE) is a significant phenomenon in modern physics and chemistry; it was first introduced in 1934 during a discussion between *L. Landau* and *E. Teller* and later developed into a fundamental approach for understanding molecular and crystal structures. This effect applies to any polyatomic system.

The core concept of JTE lies in the instability of molecular configurations in electron degenerate states, which laid the foundation for explaining various instabilities in high-symmetry molecular structures. It also helps describe the unique nuclear dynamics caused by these instabilities and the underlying reasons for structural symmetry breaking in molecular and condensed matter systems [8].

Significant progress in JTE theory began in the late 1950s, leading to major applications in spectroscopy, stereochemistry, and structural phase transitions, with research continuing for decades. Interest in this effect was revived in the late 1980s, and studies on it are still ongoing.

The Jahn-Teller theorem states that any nonlinear molecular system with electron degeneracy will be unstable and will undergo geometric distortion to achieve lower energy and reduced symmetry, thereby removing the degeneracy [9].

This effect is commonly observed in transition metal complexes, particularly in octahedral coordination compounds. A molecule or ion is considered electronically degenerate when multiple orbitals are available for a single electron. The Jahn-Teller effect is most notable in Cu^{2+} (copperII) complexes, where the d^9 electron configuration leads to an unstable electronic state. JTE theory influencing the stability of the perovskite in compounds containing transition metal ions with asymmetric valence states. This effect arises when there is electronic degeneracy in d orbitals, leading to a geometric distortion in the octahedral coordination surrounding the central metal ion [10].

The type of distortion depends on the occupancy of the d orbitals. If the d_(z^2) orbital is occupied, the structure undergoes elongation along the z-axis, whereas occupation of the d_(x^2-y^2) orbital results in compression in the horizontal plane. These distortions play a key role in determining the structural stability of perovskite materials, as they influence electronic interactions, overall energy, and electrical conductivity [11].

I.4.2 Glazer Notation for Octahedral Tilts

In 1972, Glazer introduced a widely used classification system to describe the different possible tilting patterns of BO_6 octahedra in perovskite structures. This classification defines 23 distinct tilt systems based on rotational behaviors of the octahedra.

To organize these systems, Glazer proposed a symbolic notation that refers to rotations around the three principal axes of the cubic prototype unit cell. These axes are labeled **a**, **b**, and **c** corresponding respectively to rotations around the **x**, **y**, and **z** directions [12].

When equal rotations occur around two or more axes, the same letter is repeated (e.g., $a^-a^-a^-$). The superscripts provide details about the phase relationship of the tilts between neighboring octahedra:

- **"0"** indicates no rotation around that axis.
- **"+"** denotes **in-phase** tilting between adjacent octahedra (they rotate in the same direction).
- **"-"** denotes **anti-phase** tilting (they rotate in opposite directions) [13].

This notation helps describe how the octahedra behave and tilt throughout the structure.

In recent developments, Howard and Stokes have refined the classification of possible octahedral rotation patterns in perovskite structures to 15 distinct systems. These configurations are based on the different ways in which BO_6 octahedra can rotate around the crystallographic axes. Moreover, they established a clear correlation between each tilt system and its corresponding space group, providing a systematic framework for understanding symmetry changes in perovskites [14].

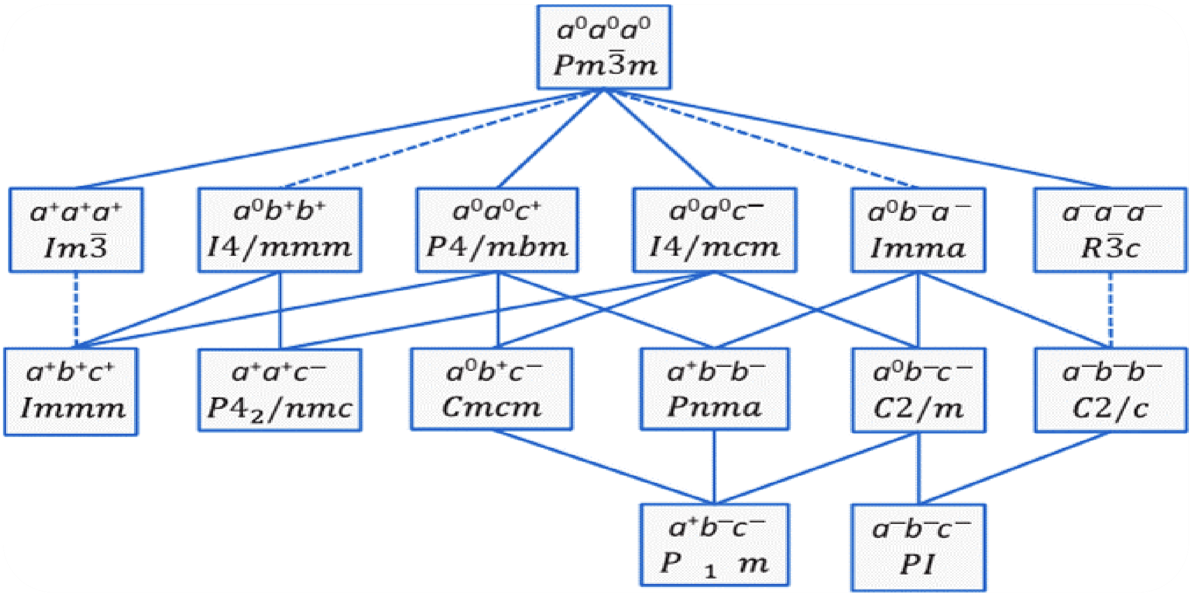

Figure 1.5. A schematic diagram indicating the group- subgroup relationships among the 15 space groups tabulated by Howard & Stokes (1998). A dashed line joining a group with its subgroup indicates that the corresponding phase transition is required by Landau theory to be first order

I.5 Families of perovskite

ABX3 perovskites are classified into the oxide family and the halogen family based on the type of element present at the X site:

- **The Family of Oxides:** with the formula ABO3, because the family of perovskites contains a large number of oxides.
- **The halogen family:** represent the elements of the seventh column of group A of the periodic table (*F, I, Br, Cl*), halide perovskites have quite outstanding properties of photoconductivity as reported in 1958 by Moller for Cesium halide perovskite $CsPbX_3$ and later on in 1978 by Weber for the hybrid organic-inorganic lead halide perovskites $CH_3NH_3PbX_3$ [15].

I.6 Types of perovskites

I.6.1 Tetragonal perovskite

The most well-known example of a tetragonal perovskite is probably the ferroelectric form of $BaTiO_3$ at room temperature, with a = 3.994 Å, c = 4.038 Å, and Z = 1. In this case, the TiO_6 octahedra are slightly distorted (one Ti-O bond at 1.86 Å, four at 2.00 Å, and one longer at 2.17 Å). Barium is coordinated by four oxygens at 2.80 Å, four at 2.83 Å, and four others at 2.88 Å. In the isotope $PbTiO_3$, the TiO_6 polyhedra are more distorted than in $BaTiO_3$, which may be related to a greater polarization power and the ionic radius of Pb (II), this has often been discussed in systems containing this cation [16].

I.6.2 Rhombohedral Perovskite

In several materials, the cubic lattice can have a slight distortion to rhombohedral symmetry. If this deformation does not expand the unit cell, it is possible to index it to another cell containing one or two unit formulas respectively with rhombohedral angles $\alpha \approx 90°$ or $\alpha \approx 60°$. However, the anions are generally displaced as required by the larger unit cell with $\alpha = 60°$. Examples of rhombohedral perovskites are: $LaAlO_3$, $PrA1O_3$, $LaNiO_3$, and $LaCoO_3$. $LaCoO_3$ has a rhombohedral structure at room temperature, but at high temperatures, it undergoes two interesting phase transitions, transforming into another rhombohedral phase (R3c to R3). Also, the trivalent cobalt is ordered in such a way as to have an alternation of (111) planes with high-spin and low-spin of Co (III) ions. Above 937°C, a second transition occurs, in which the space group R3 is maintained but the angle changes abruptly from 60.4° to 60.0° [17].

I.6.3 Orthorhombic Perovskite

The structure $GdFeO_3$ is probably the most illustrative of all distorted orthorhombic perovskites, its space group is Pbnm and its lattice parameters are: a = 5.346Å, b = 5.616Å, and c = 7.666Å with Z = 4. These are related to the pseudo-cubic lattice: $a \sim b \sim \surd 2a_0$ and $c \sim 2a_0$ [49]. In this structure, the FeO_6 octahedra are distorted and tilted. Furthermore, the GdO_{12} polyhedron is severely distorted, showing (8 + 4) coordinations. Other materials adopting this distorted orthorhombic structure include $NaUO_3$, $NaMgF_3$, $LaYbO_3$, and a large number of lanthanide compounds of the type $LnCrO_3$, $LnGaO_3$, $LnFeO_3$, $LnMnO_3$, $LnRhO_3$, etc [18].

I.7 Crystalline structure of double perovskite

Double perovskite halides can be considered as two simple perovskites (ABX_3) and ($A'B'X_3$) alternated along the three crystallographic directions. They were first proposed by *Ward* and *Longo* in 1961[19]. Their general formula is AA'BB'X6, where A and A' can be alkali metals, alkaline earth metals, or lanthanides, and B and B' are transition metals or alkaline earth metals. Often A and A' represent the same element, and the double perovskite is represented in this case by the general formula ($A_2BB'X_6$: double perovskite ordered on the B site). Similarly, for double perovskite compounds ordered on the A site, they are represented by the general formula A $A_2BB'X_6$. For these compounds, on the B sites with coordination number 6, the two cations (B and B') alternate, surrounded by halogens, forming BX_6 and $B'X_6$ octahedra joined at the vertices, while the A cation, with coordination number 12, occupies the center of the cuboctahedron formed by them **(Fig.I.6.a).** This structure can also be seen as a cubic structure of A cations with faces centered by halogens, whose center (octahedral site) is alternately occupied by B and B' cations **(Fig.I.6.b)** [20].

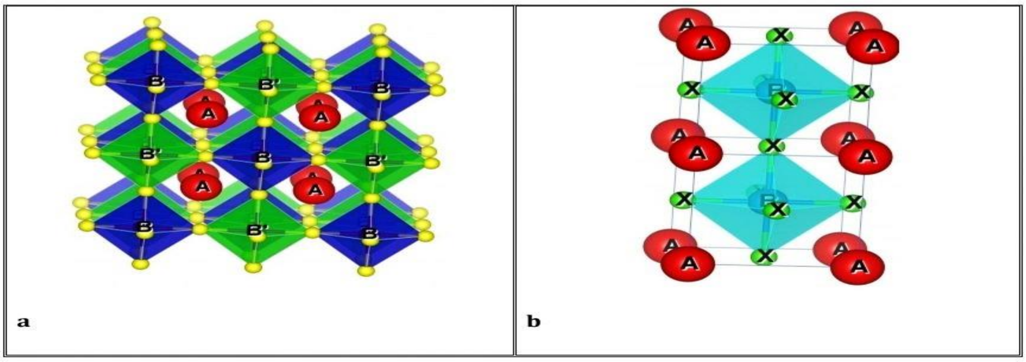

Figure I.6. Structural representation of a double perovskite $A_2BB'X_6$; a) View in the form of a network of alternating BX6 and $B'X_6$ octahedra whose cuboctahedral cavities are occupied by A cations. b) View in the form of a cubic lattice of A, whose faces are occupied by oxygen and the centers (alternate octahedral sites) by B and B'.

Temperature and pressure, which are external factors, play an essential role in the stability of simple and double perovskites. Additionally, there are two intrinsic factors: ionic radii and the difference in electronegativity between the cations and the halogen. In addition to structural asymmetries, perovskites can deviate from the ideal structure by exhibiting ionic and electronic structural defects.

I.9 Electronic properties of double perovskites

The electronic properties of perovskite oxides are largely governed by the cations at the B sites. Thanks to the diversity of cations occupying the two B sites in the structure of double perovskites $A_2BB'O_6$, these compounds can exhibit a wide range of properties such as semiconductors, metallic, half-metallic, dielectric, thermo-electric, and even superconductors. The most intriguing electrical properties are often found in materials containing different transition metals, and what is particularly interesting about $A_2BB'O_6$ perovskites is the possibility of combining 3d and 4d/5d elements of the two B sites. The electrical properties of a solid are largely governed by its band structure, as well as by the balance between interatomic interactions (described by the electronic bandwidth W) and intra-atomic electron-electron interactions (U). In the case of an empty conduction band (for example, in d0 transition metal oxides), the compounds are insulators. With a partially filled conduction band, electrons are localized when $W < U$, and they can be itinerant when $W > U$. The electronic bandwidth of a perovskite $\mathrm{A_2BB'O_6}$ largely depends on the overlap between the orbits of its different elements, which, in turn, strongly depends on the crystal structure. The W band can be estimated using two parameters: the angle between the bonds and their lengths [21, 22]. In general, this band is narrow in perovskites with a 3d transition metal on the B site, due to the relatively contracted nature of the 3d orbitals and the corresponding weak overlap with the O (2p) orbitals, particularly in the π bonds. For the same reason, the inter-electronic repulsion in 3d metals is often notable, so $W < U$ is often found. In contrast, the 4d/5d orbitals are generally more extended and, consequently, the bandwidth is often greater in compounds where the B-site cation is a 4d/5d transition metal [23].

In these compounds, spin relocation is more commonly observed. In ordered double perovskite compounds (ODPC), this relocation phenomenon can be partially inhibited by the other cation at the B' site. In these compounds, in addition to spatial overlap, energy overlap and the symmetry of the orbitals of the two cations at the B and B' sites must also be taken into account. Generally, electron itinerancy in ODPCs only becomes possible in relatively rare cases with good orbital energy overlap and correct symmetries, and these factors explain why few $A_2BB'O_6$ compounds exhibit metallic character [24].

I.10 Property of half-metallicity

Half-metallicity is the most coveted characteristic in ODPCs, and simultaneously, it is arguably the most fascinating. Half-metallicity is challenging to detect experimentally. It is susceptible to cation disorder and spin-orbit coupling (SOC). Half-metals are typically metallic compounds exhibiting a half-integer spin moment at absolute zero (0 K) [25]. The A_2FeMoO_6 compounds (where A = Ca, Sr, Ba) are the most extensively researched half-metallic $A_2BB'O_6$ perovskites. All exhibited half-metallic characteristics, demonstrating elevated metallic conductivity and significant tunnel magnetoresistance (TMR) behavior, even at ambient temperature.

I.11 Magnetic properties of double perovskites

The magnetic characteristics of oxides are contingent upon the spatial orbital overlap of their constituent ions, which is influenced by the structural configuration. The overlap that generates superexchange interactions is not the sole mechanism influencing magnetic order; electron hopping, akin to the double exchange interaction, also plays a significant role [26]. Double perovskites $A_2BB'O_6$ provide diverse magnetic phenomena owing to the potential for integrating various paramagnetic cations across the three cation sites. While numerous compounds in this family exhibit antiferromagnetic (AFM) properties, it also includes a significant number of ferromagnetic (FM) or ferrimagnetic (FiM) compounds, some possessing exceptionally high Curie temperatures (Tc). In the presence of a solitary paramagnetic cation at site B, super-exchange interactions transpire across an extended distance. The interaction forces between nearest neighbors (NN13) at 90° (B-O-B'-O-B) are frequently comparable in magnitude to those between next nearest neighbors (NNN14) at 180° (B-O-B'-O-B) and may compete with them [27], [28]. Typically, they exhibit greater strength when the d-eg orbitals of cation B are unoccupied, and diminished strength when these orbitals are half-filled [29]. When two magnetic cations occupy the B site, the orbital energy overlap between them is frequently inadequate. Consequently, it may be reasonably prevalent for the long-range super-exchange interactions B-O-B'-O-B or B'-O-B-O-B' (NNN) to surpass the strength of the short-range contact B-O-B' (NN) in these compounds. A paramagnetic cation may coexist on site A concurrently with site B (e.g., Mn_2FeSbO_6). In this instance, magnetic coupling may exist between sites A and B, as the spins of Mn and Fe are interconnected [30]. Paramagnetic ions may occupy all three cationic sites (e.g., Nd_2MnNiO_6), exhibiting magnetic coupling among the cations, despite the typically weaker coupling between sites A and B (Mn and Ni are ferromagnetically aligned at 200K, whereas Nd is antiferromagnetically oriented at site B at 45K) [31], [32].

I.11.1 Diamagnetism

Diamagnetism in matter arises from alterations in electron motion prompted by the introduction of a magnetic field. According to Lenz's law, these alterations typically counteract the originating cause. All atoms and molecules possess inherent demagnetization, which contributes negatively to magnetic susceptibility. This contribution is typically feeble and obscured by the presence of paramagnetic. The examination of diamagnetism is thus especially significant for atoms or ions possessing complete electron shells [33]. Diamagnetism defines materials composed only of non-magnetic atoms. The susceptibility is mostly unaffected by the field and temperature **(Fig.I.7),** is negative, and typically measures around [34]. Diamagnetism results from Lenz's law, which asserts that alterations in the magnetic flux within a current loop, due to an external magnetic field, generate induced currents that correspond to an induced moment at the atomic level. Lenz's law states that induced currents generate an induction flux that opposes the change in the applied field. This magnetism is present in material containing magnetic atoms; however, it is so feeble that it is entirely obscured by the influence of the magnetic atoms.

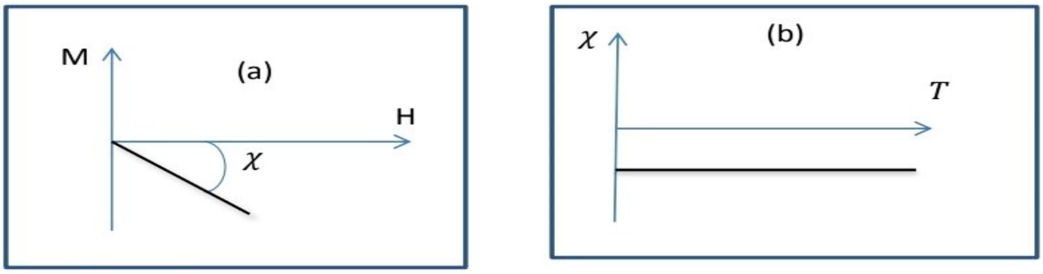

Figure I.7. (a) Variations of magnetization in response to a magnetic field. (b) Thermal variation of magnetic susceptibility.

I.11.2 Paramagnetism

In this magnetic phase, the fundamental magnetic moments are oriented randomly in all directions because of thermal agitation. At temperatures exceeding the transition temperature (Curie for ferromagnetism or Néel for antiferromagnetism), thermal energy surpasses magnetic interaction energy, which influences the configuration of magnetic moments. The substance exhibits 0% magnetization until subjected to an external magnetic field. In numerous instances, the magnetism of paramagnetic materials arises from the permanent magnetic moments possessed by all or some of the atoms. The moments exhibit minimal interaction, leading to the discussion of the paramagnetism of unbound atoms **(Fig.I.8.a).** The application of a magnetic field alters the average orientation of the moments, resulting in an induced magnetization that aligns parallel to the field. The magnetization diminishes with increasing temperature, indicating substantial thermal agitation **(Fig.I.8.b).** The rise in temperature amplifies the fluctuations in magnetization relative to the field, resulting in a progressively linear relationship. The initial susceptibility, positive, is unlimited at absolute zero and diminishes as the temperature rises. It typically ranges from 10^-3 to 10^-5 at ambient temperature [35]. In an optimal scenario, the inverse of the initial susceptibility varies in direct proportion to temperature, as described by the Curie law **(Fig.I.8.c).**

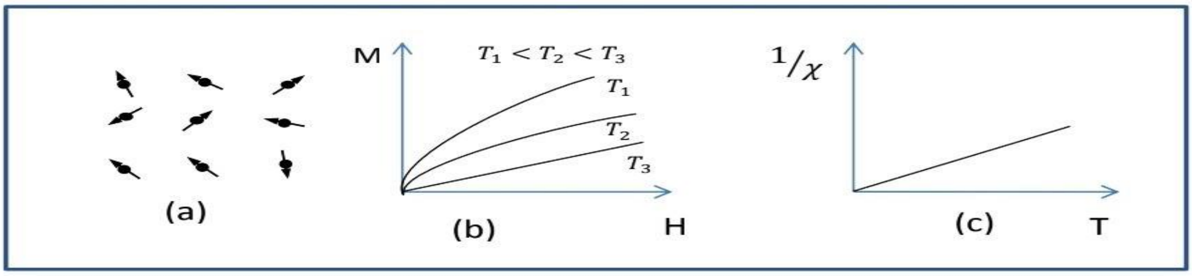

Figure I.8. Paramagnetism of Isolated Atoms.

I.11.3 Antiferromagnetism

A simple antiferromagnet can be seen as two magnetic sublattices (A and B). In the magnetically ordered state, the atomic moments are coupled in parallel in each of the two sublattices. Two atomic magnetic moments belonging to different sublattices have an antiparallel orientation. Given that the moments of the two sublattices have the same value and are oriented in opposite directions, it is observed that the total magnetization of an antiferromagnet is essentially zero (at least at zero Kelvin) [36]. Antiferromagnetism is a weak magnetism similar to paramagnetism because the susceptibility is low and positive. However, the thermal variation of the inverse susceptibility, measured on a polycrystalline substance, presents a minimum of the temperature known as the Néel temperature TN **(Fig.I.9.c).**

This maximum susceptibility originates from the appearance, below TN, of an antiparallel arrangement of the magnetic moments present in the substance, which, in the simplest cases, divide into two sub-lattices of equal and opposite magnetizations so that in the absence of a field, the total magnetization is zero **(Fig.I.9.a).** This antiparallel arrangement of individual moments is the consequence of interactions between neighboring atoms (called negative exchange interactions). These oppose the action of the applied field, which would tend to make the moments parallel. When the temperature decreases below TN, the susceptibility decreases because the thermal agitation that opposes the antiferromagnetic order of the moments decreases. At high temperatures, thermal agitation takes over and we observe a thermal variation of susceptibility similar to that of a paramagnet **(Fig.I.9.b and c).** We have presented here the simplest case of antiferromagnetism, consisting of two antiparallel sublattices. In fact, there are many antiferromagnetic substances that exhibit more complex magnetic structures, particularly non-collinear ones [36].

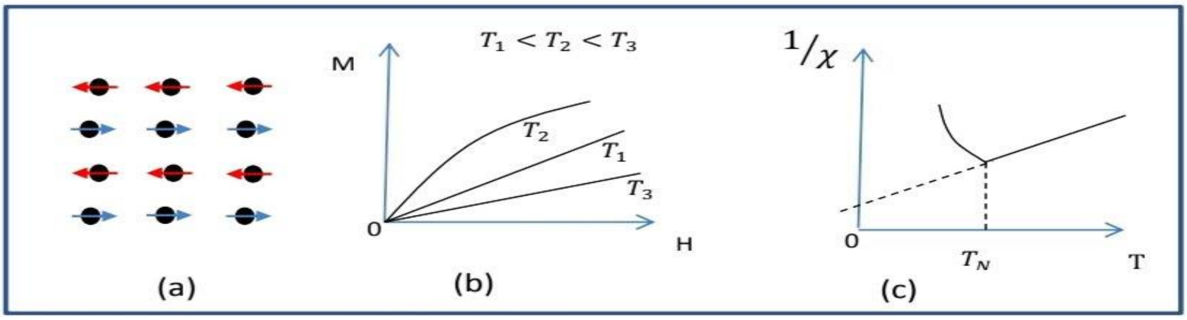

Figure I.9. Antiferromagnetism: (a) spin lattice; (b) M=f(H); (c) 1/X ~(T)

I.11.4 Ferromagnetism

A ferromagnetic material exhibits spontaneous magnetization at low temperatures, indicating that the sum of its magnetic moments is non-zero even without an external magnetic field, in contrast to the prior scenario. Positive exchange interactions facilitate the parallel alignment of the magnetic moments of adjacent atoms in a ferromagnetic material **(Fig.I.10).** Subsequently, events transpire as though a magnetic field, termed a molecular field, aligns the moments; this hypothetical field is crucial in elucidating ferromagnetism, but it does not constitute an actual magnetic field. Similar to antiferromagnetism, at elevated temperatures, thermal agitation results in a susceptibility akin to that of a paramagnet, as illustrated by the Curie-Weiss law in **(Fig.I.10.c).** Nevertheless, owing to magnetic interactions, the susceptibility does not become infinite at 0 K as observed in a paramagnet; rather, it becomes infinite at a certain temperature known as the Curie temperature (Tc). Below this temperature, interactions prevail over thermal agitation, resulting in the emergence of spontaneous magnetization (Ms) in the absence of an external field. The magnetization attains its peak value MO at absolute zero, indicative of the parallel alignment of all individual moments **(Fig.I.10.b and d).**

Despite the existence of spontaneous magnetization below TC, a piece of ferromagnetic material is not necessarily spontaneously magnetized: its magnetic moment can be zero, in which case the material is said to be demagnetized. This stems from the fact that the interior of the material is separated into magnetic domains, called Weiss domains; each domain, which contains a significant number of atoms, is spontaneously magnetized. From one domain to another, the direction of the moments fluctuates so that the total magnetic moment of the sample is zero. Nonetheless, the application of a field alters the distribution of the domains, leading to a change in magnetization . Consequently, at the macroscopic scale, a ferromagnetic material is a substance that typically attains significant magnetization in response to an external magnetic field [37]. In the presence of sufficiently strong magnetic fields, magnetization typically reaches saturation.

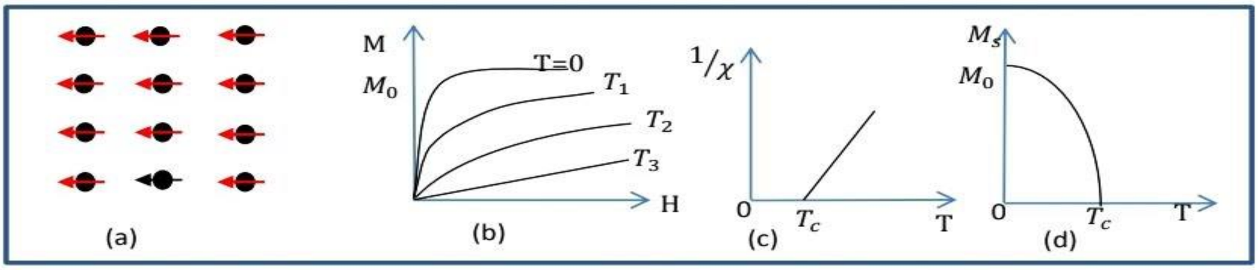

Figure I.10. Ferromagnetism: (a) Spin lattice; (b) Magnetization variation under an external field (Tj < Tc < T2 < T3); (c) Thermal variation of (1/X); (d) Thermal variation of spontaneous magnetization.

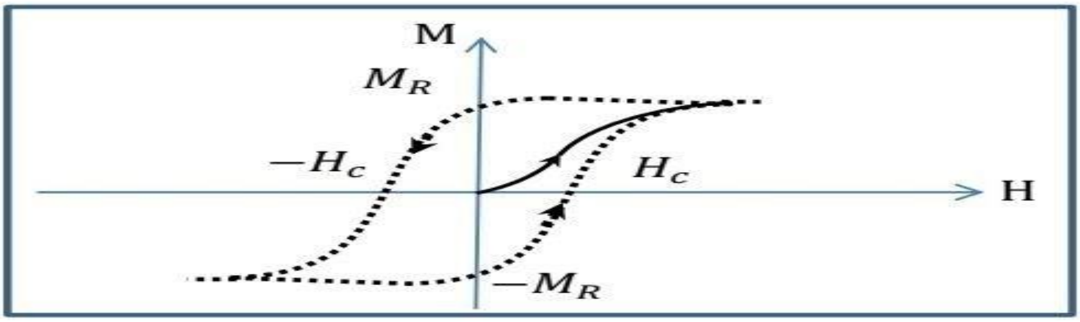

Figure I.10. Magnetization curve of an unmagnetized material or initial magnetization curve (solid line) - Hysteresis loop (dashed lines)

I.11.5 Ferrimagnetism:

Ferrimagnetism defines a material of the antiferromagnetic variety wherein the two sublattices exhibit unequal magnetization **(Fig.I.11.a)**: the magnetization of the two sublattices is no longer perfectly compensated. Consequently, below the ordering temperature TC, spontaneous magnetization arises, resulting in macroscopic properties of a ferromagnetic material in this temperature range that closely mirror those of a ferromagnetic material **(as illustrated in Fig.I.11 b and d).**

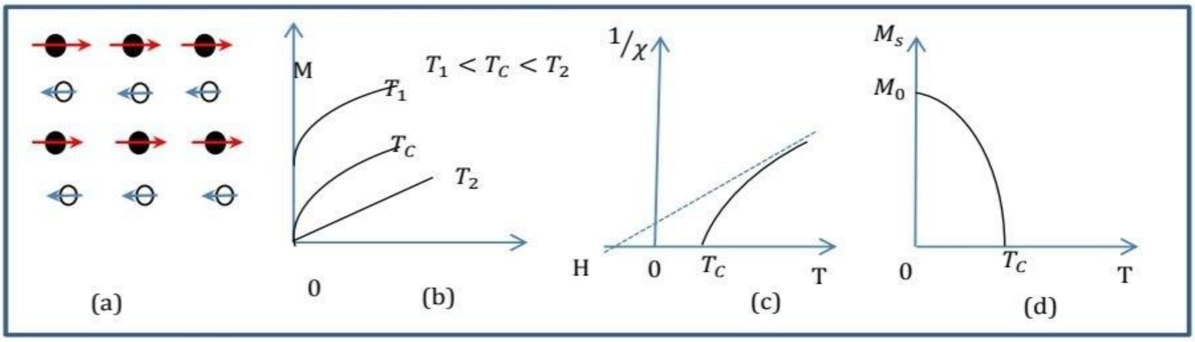

Figure I.11. Ferrimagnetism: (a) Spin lattice; (b) Thermal variation of 1/x; (d) Thermal variation of spontaneous magnetization; (c) Variation of magnetization under a magnetic field.

Inverse of the magnetic susceptibility begins to depart substantially from its essentially linear behavior at extremely high temperatures [21]. In contrast to ferromagnetic materials, the area of negative temperatures is where the asymptote of the curve 1/x = f(T) contacts the x-axis **(Fig.I.12.c).** Substances can be categorized as ferromagnetic or ferromagnetic if they display non-collinear magnetic structures and/or contain many types of magnetic atoms with varying moments.

I.12 Perovskite Materials: Their Uses and Applications

Perovskite structures, with their inherent flexibility and diverse compositions, have emerged as integral components in modern electronics, and the following examples show the practical applications of double perovskites in various contexts.

I.12.1 Fuel Cells Made of Solid Oxide (SOFC)

Fuel cells represent a viable way to mitigate environmental issues, particularly global warming resulting from greenhouse gas emissions. Ba_2LnBO_6 double perovskites demonstrate promise as anode materials in solid oxide fuel cells, intended for stationary applications at elevated temperatures reaching 1000°C. These fuel cells, referred to as combined heat and power systems, can attain remarkable efficiency, reaching up to 70%, according to studies [38][39].

I.12.2 Photovoltaic Devices

In recent years, there has been a growing interest in photovoltaic (PV) systems that directly convert sunshine into electrical energy. These systems are acknowledged as essential solutions to meet increasing energy demands, utilizing plentiful solar resources [40]. Although silicon (Si) and gallium arsenide (GaAs) have historically been preferred materials for solar cells, halide perovskites, exhibiting enhanced photovoltaic properties, have garnered significant interest [41]. Nonetheless, their susceptibility to external factors hinders practical integration. Conversely, oxide perovskites and their derivatives, recognized for superior stability, are more widely utilized in solar systems [40] [42] [43].

I.12.3 Devices by Spintronics

Traditional electronics depend on the use of electric charges to manipulate information. Spintronics, a nascent discipline, amalgamates electronics with magnetism by utilizing the intrinsic magnetic moment of electrons, referred to as spin [44]. In spintronics, the manipulation of both the charge and spin characteristics of electrons is essential for information transmission. Applications encompass spintronic heads in hard drives and non-volatile electronics [45]. Current emphasis is on investigating innovative half-metallic magnetic materials for spintronics, such as ferrimagnetic double perovskites like Sr_2CrReO_6.

I.13 Conclusion

In conclusion, perovskite materials are among the important materials in modern industries due to their unique properties, especially in fields such as solar cells, electronics, and semiconductors. A deep understanding of their structure and physical and chemical properties can open up wide horizons for innovative future applications, making them a significant focus in contemporary scientific and technological research.

1. B.venugopal, S.H. rochna and N. hariprachad. « Perovskite materials- AN INTRODUCTION» , Indian Institute of Technology Madras 2019 .
2. BENAISSA CHERIF, Y. (2008). « *Structures Magnétiques des Pérovskites de type ABC3 Etude du premier principe* ». Thèse en science. Université de Mostaganem.
3. Miller, S, C and Love, W, F. (1967). Tables of Irreducible Representations of Space Groups.
4. ADJAL, M & HOURI, N. (2022). *« Les structures pérovskites en feuillets»*. Université de Biskra.
5. Fermi, E and Phys, Z.(1928), p. 73
6. Travis, W *et al.,* (2016). On the application of the tolerance factor to inorganic and hybrid halide perovskites: a revised system. *Chem. Sci*, 7, 4548.
7. Sonnati, M. (2011). La Chimie Orga en 3 mois, 6 (47).
8. Mandeep, D. A Textbook of Physical Chemistry – Volume 1.
9. SOUIDI, A. (2017). Thèse de doctorat. *« Etude des Propriétés Spintroniques du Double Pérovskite Type ABCO6 ».* Université de Mostaganem.
10. Jahn, H, A *et al.,* (1937). London, A161, 220.
11. ISAAC, B. BERSUKER. (2006). "*The jahn–teller effect".* The University of Texas at Austin.
12. Cryst, A. (1998). Group-Theoretical Analysis of Octahedral Tilting in Perovskites.
13. Christopher, J and Stokes, H, T. A Australian Nuclear Science and Technology Organisation, Private Mail Bag 1, Menai NSW 2234, Australia, and b Department of Physics and Astronomy, Brigham Young University, Provo, Utah 84602-4675, USA.
14. Crystallographica, A. (2002). Section B Structural Science, research papers, Group-theoretical analysis of octahedral tilting in ferroelectric perovskites, Harold T. Stokes, a Erich H. Kisi,b Dorian M. Hatcha and Christopher J. Howardc,d.
15. Crystallographica, A. (2004). Section B Structural Science , research papers , Octahedral tilting in cation-ordered perovskites ± a group-theoretical analysis, Christopher J. Howarda,b* and Harold T. Stokes.

16. Y. Yuan , Z *et al,*. (2014). Huang arising applications of ferroelectric materials in photovoltaic devices , journal of materials chemistry A , vol . 2 , pp . 6067-6041.
17. Jemli, M, K. (2016). « *Synthèse et auto-assemblage des molécules de perovskites pour la photonique et le marquage* ». Thèse de doctorat. Université Paris.
18. Tlili, M *et al,*. (2011). Materials Characterization 6 2, 243.
19. Miller, S and Love, W, F. (1967). Tables of irreducible representations of space groups and co-representations of magnetic space groups: Pruett Press.
20. Longo, J and Ward, R. (1961). *"Magnetic compounds of hexavalent rhenium with the perovskite-type structure".* Journal of the American Chemical Society, vol. 83, pp. 2816 2818.
21. Paier, M *et al,*. (2006). Phys., Vol. 125, p. 249901.
22. Aulbur, M and Städele and A. Görling. (2000). Phys. Rev., Vol. B 62, p. 7121.
23. Faleev, S *et al,*. (2004). Phys. Rev. Lett., Vol. 93, p. 126406.
24. Gerl, M and Issi, J-P. (1997). Traité des Matériaux volume 8, Physique des Matériaux, Presses Polytechniques et Universitaires Romandes.
25. Coey, J and Venkatesan, J. (2002). Appl. Phys., Vol. 91, p. 8345.
26. Serrate, J *et al,*. (2007). Phys. Condens. Matter, Vol. 19, p. 023201, 2007.
27. Blasse, G. (1965). Philips Res. Reports, Vol. 20, p. 327.
28. Singh, R and Tomy, C, V. (2008). Phys. Rev., B Vol. 78, p. 24432
29. Tomioka, Y *et al,*. (2000). Phys. Rev., Vol. B 61, p. 422.
30. Santos-García, A, D *et al,*. (2013). Phys. Condens. Matter, Vol. 25, p. 206004, 2013.
31. Asai, K. *et al,*. (1998). Phys. Soc. Jpn., Vol. 67, p. 4218.
32. Sánchez-Benítez, J *et al,*. (2011). Phys. Condens. Matter, Vol. 23, p. 226001.
33. Gerl, M and Issi, J, P. (1997). Physique des matériaux vol. 8: PPUR presses polytechniques.
34. Buschow, K and Boer,F. (2003). Physics of magnetism and magnetic materials vol. 7: Springer.
35. Kittel, C *et al,*. (1983). Physique de l'état solide vol. 7: Dunod. France.

36. Smart, L. (1997). « *Introduction à la chimie du solide ».*

37. Vajda, P and Andre, G. (2001). *"Commensurate and incommensurate magnetic structures in rare-earth hydrides".* Journal of alloys and compounds, vol. 326, pp. 151-156.

38. Niu, B *et al,.* (2019). *"Highly carbon and sulfur tolerant Sr2TiMoO6 -δ double perovskite anode for solid oxide fuel cells"*. International Journal of Hydrogen Energy, 44(36):20404–20415.

39. Flores, J *et al,.* (2021). "Advances in the knowledge of the double perovskites derived from the conformation and substitution of the material Sr2MgMoO6 -δ as anode with potential application in sofc cell". International Journal of Hydrogen Energy, 46(51): 26152–26162.

40. Yin, W *et al,.* (2019). "Oxide perovskites, double perovskites and derivatives for electrocatalysis, photocatalysis, and photovoltaics". Energy & Environmental Science, 12(2):442–462.

41. Stranks, SD and Snaith, HJ. (2015). "Metal-halide perovskites for photovoltaic and lightemitting devices". Nature nanotechnology, 10(5):391–402.

42. Sheikh, M *et al,* (2017). "*Lead free double perovskite oxides ln2nimno6 (Ln La,Eu,Dy,Lu), a new promising material for photovoltaic application".* Materials Science and Engineering: B, 226:10–17.

43. Sun, Q *et al,.* (2018). *"Bandgap engineering of stable lead-free oxide double perovskites for photovoltaics".* Advanced Materials. 30(15):1705901.

44. Pearton, SJ *et al,.* (2006). *"Zno spintronics and nanowire devices".* Journal of electronic materials, 35:862–868.

45. Felser, C and Fecher, GH. (2013). "*Spintronics: from materials to devices*". Springer Science & Business Media.

Chapter 2: Density Functional Theory (DFT)

II.1 Introduction

Condensed matter Physics and materials science are fundamentally concerned with the understanding and exploitation of the properties of interacting electron and atomic nucleus systems. This has been well known since the development of quantum mechanics. With this comes the recognition that at least almost all properties of materials can be studied using computational tools suitable for solving this particular problem of quantum mechanics. Unfortunately, the electrons and nuclei that make up materials constitute a strongly interacting many-body system, and this makes the solution of the Schrödinger equation extremely difficult. As Dirac stated (in 1929), progress depends on the development of sufficiently accurate approximate techniques. Thus, the development of density functional theory (DFT) to describe a material. We need to know these properties (electronic, structural, optical...). And this involves understanding the interactions between the electrons and ions that constitute it, but in this case, classical mechanics proves to be insufficient, and quantum mechanics must be invoked, the foundation of which is the solution to the Schrödinger equation.

II.2 The Schrödinger equation of a crystalline solid

Let us consider a material system consisting of n electrons and N atomic nuclei. All the information is contained in the wave function, which is governed by the time-independent Schrödinger equation:

$$\mathbf{H\Psi = E\Psi} \qquad \textbf{(II.2.1)}$$

Where:

H: Hamiltonian operator which includes the kinetic energy and the potential energy of the particles.

Ψ: The wave function of the system.

E: The total energy of the crystal.

Generally, the Hamiltonian operator is written as:

$$\mathbf{H = T_e + T_n + V_{e-e} + V_{n-n} + V_{e-n}} \qquad \mathbf{(II.2.2)}$$

Where:

The kinetic energy of the electrons Te:

$$\boldsymbol{T_e} = \sum_{i=1}^{N} \frac{\boldsymbol{P_i^2}}{\boldsymbol{2m_e}} = \sum_{i=1}^{N} \frac{-\hbar^2}{\boldsymbol{2m_e}} \Delta_i \qquad \textbf{(II.2.3)}$$

The kinetic energy of the nuclei:

$$\boldsymbol{T_n} = \sum_{i=1}^{n} \frac{\boldsymbol{P_i^2}}{\boldsymbol{2M_n}} = \sum_{i=1}^{n} \frac{-\hbar^2}{\boldsymbol{2M_n}} \Delta_i \qquad \textbf{(II.2.4)}$$

The electron-electron interaction potential:

$$\boldsymbol{V_{e-e}} = \frac{1}{2} \cdot \frac{1}{4\pi\varepsilon_0} \sum_{i \neq j} \frac{e^2}{|\vec{r_i} - \vec{r_j}|} \qquad \textbf{(II.2.5)}$$

The nucleus-nucleus interaction potential:

$$\boldsymbol{V_{n-n}} = \frac{1}{2} \cdot \frac{1}{4\pi\varepsilon_0} \sum_{\alpha \neq \beta} \frac{Z_\alpha Z_\beta e^2}{|\vec{R_\alpha} - \vec{R_\beta}|} \qquad \textbf{(II.2.6)}$$

The nucleus-electron interaction potential:

$$\boldsymbol{V_{e-n}} = -\frac{1}{4\pi\varepsilon_0} \sum_{i,\alpha} \frac{Z_\alpha e^2}{|\vec{r_i} - \vec{R_\alpha}|} \qquad (\mathrm{II.2.7})$$

$\vec{r_i}$ Represents the coordinates of the electrons.

$\vec{R_\alpha}$ Are the coordinates of the nuclei.

The wave function depends on the coordinates of all the particles, that is:

$$(\boldsymbol{T_e} + \boldsymbol{T_n} + \boldsymbol{V_{e-e}} + \boldsymbol{V_{n-n}} + \boldsymbol{V_{e-n}})\boldsymbol{\Psi}(\vec{r_1}, \vec{r_2}, .. \vec{R_1}, \vec{R_2} ..) = \mathrm{E}\boldsymbol{\Psi}(\vec{r_1}, \vec{r_2}, ... \vec{R_1}, \vec{R_2} ..) \qquad \textbf{(II.2.8)}$$

All observable properties of the electron-nucleus system are contained in equation (I.2). It is sufficient to solve the equation to obtain its physical and chemical properties.

However, solving the Schrödinger equation for a system of interacting bodies is very complicated. For poly-electronic systems, the equation contains variables, so it is necessary to resort to approximation methods to solve the Schrödinger equation in an approximate manner. The three main levels of simplification generally used are:

The Born-Oppenheimer approximation or adiabatic approximation.

II.3 The Born-Oppenheimer Approximation

This approximation is based on the fact that the mass of any nucleus is significantly greater than that of the electron. For this reason, the motion of the nuclei relative to the electrons can be neglected. Consequently, it is assumed that the electrons evolve in a potential created by fixed atoms. In this context, the kinetic energy of the nuclei ($T_n = 0$) and the Coulomb energy (V_{n-n} due to the repulsion between the nuclei) becomes a constant. At this stage, we move from a problem in which we had to solve the Schrödinger equation for a system of N electrons + M nuclei, to solving the Schrödinger equation for a system of N electrons experiencing the potential of the nuclei. Therefore, the Hamiltonian of the electrons is given by:

$$\boldsymbol{H_e = T_e + V_{e-e} + V_{e-n}} \qquad \textbf{(II.3.1)}$$

$$\boldsymbol{H_e = \sum_{i=1}^{N} \frac{-\hbar^2}{2m_e}\Delta_i + \frac{1}{2}\cdot\frac{1}{4\pi\varepsilon_0}\sum_{i\neq j}\frac{e^2}{|\vec{r_i}-\vec{r_j}|} - \frac{1}{4\pi\varepsilon_0}\sum_{i,\alpha}^{n}\frac{Z_\alpha e^2}{|\vec{r_i}-\vec{R_\alpha}|}} \qquad \textbf{(II.3.2)}$$

The electronic Schrödinger equation can then be written as:

$$\mathbf{H_e\psi = E_e\psi} \qquad \textbf{(II.3.3)}$$

$\boldsymbol{E_e}$**:** represents the energy of the electrons moving in the field created by fixed nuclei.

Despite these simplifications, solving this equation remains extremely difficult because for a system with n electrons, it depends on 3n spatial coordinates. This is why it is very often combined with the Hartree approximation [3].

II.4 The-Hartree-Fockapproximation

In 1927, Hartree proposed a method for calculating approximate poly-electronic wave functions by expressing them as products of mono-electronic wave functions [3]. To each electron corresponds an orbital, and the total wave function is written as a product of one-particle wave functions, orthogonal to each other:

$$\boldsymbol{\Psi = \Psi_1(r_1).\Psi_2(r_2).\Psi_3(r_3)\,.....\,\Psi_N(r_N)} \qquad \textbf{(II.4.1)}$$

In 1930, Fock corrected Hartree's method, which does not respect the antisymmetry principle of the wave function [4]. Indeed, according to the Pauli exclusion principle [5], two electrons cannot be simultaneously in the same quantum state. The Hartree-Fock method [6] allows an approximate solution of the Schrödinger equation for a quantum system with n electrons and N nuclei, in which the poly-electronic wave function Ψ_{HF} is written in the form of a Slater determinant [7] composed of single-electron spin orbitals that respect the antisymmetry of the wave function:

$$\boldsymbol{\psi} = \frac{1}{\sqrt{N!}}\begin{vmatrix} \psi_1(\vec{r}_1)\psi_1(\vec{r}_1)...\psi_1(\vec{r}_1) \\ \psi_2(\vec{r}_2)\psi_2(\vec{r}_2)...\psi_2(\vec{r}_2) \\ \vdots \quad\quad \vdots \quad\quad \vdots \\ \psi_N(\vec{r}_N)\psi_N(\vec{r}_N)\,....\,\psi_N(\vec{r}_N) \end{vmatrix} \tag{II.4.2}$$

$\frac{1}{\sqrt{N!}}$ is a normalization factor [8]:

This determines which allows calculating the wave functions and minimizing the total energy with respect to the mono-electronic wave functions ψ_i.

.We thus reduce it to a single-electron wave equation, which is a generalization of the Hartree equation:

$$\left[-\frac{\hbar^2}{2m_e}\nabla^2 + V_{ext}(\vec{r}) + V_H(\vec{r}) + V_X(\vec{r})\right]\psi_i(\vec{r}) = E\psi_i(\vec{r}) \tag{II.4.3}$$

$V_x(\vec{r})$is the Fock term [8] defined by its action on a wave function $\psi_i(\vec{r})$:

$$V_x(\vec{r})\psi_i(\vec{r}) = -\sum \delta_{\sigma_i\sigma_j}\,\psi_j(\vec{r})\int \frac{\psi_j^*(\vec{r})\psi_i(\vec{r})}{|\vec{r}-\vec{r}'|}\,d^3\overrightarrow{r'} \tag{II.4.4}$$

II.5 The Density Functional Theory (DFT)

II.5.1 Origin of the DFT

Using density as a variable instead of the wave function is the idea that was suggested by Thomas and Fermi in 1927 [9,10].They proposed to model the kinetic term of the Schrödinger equation using a specific functional explicitly based on the density.The weak point of this approach lay in the expression of the kinetic energy, which did not take into account atomic orbitals (it does not allow for the explanation of covalent bonding, for example), and the precision obtained was also inferior to that of Hartree-Fock due to the absence of the exchange term.Dirac improved this theory by adding to it an exchange energy functional of the electronic density, but the electronic correlation term remained absent in this new approach.Nevertheless, using density leads to simpler resolutions than in the case of the wave function.The Hohenberg-Kohn approach established a rigorous framework that allows for the elimination of any approximation.

II.5.2 The Thomas-Fermi approximation:

The density functional theory has its origins in the Thomas-Fermi model.Shortly after the formulation of the laws of quantum mechanics, Thomas and Fermi (1927) [9,10] had already attempted to express the kinetic energy and the exchange and correlation energy of the homogeneous electron gas to construct the same quantities for the inhomogeneous system in the following way:

$$\boldsymbol{E_\alpha = \int E_\alpha\,[\rho(r)]dr} \qquad \textbf{(II.5.1)}$$

Where $E_\alpha[\rho(r)]$r represents the energy density corresponding to the portion α for the homogeneous electron gas, this method relies on a statistical model to approximate the electronic distribution around an atom.The mathematical basis used was to postulate that the electrons are distributed uniformly in phase space, in each volume V = l^3 we have a fixed number of electrons N, and we assume that the electrons in each cell are independent fermions at 0 K [11]. For each volumetric element d^3r, it is possible to fill a momentum space sphere up to the Fermi radius pf [12]:

$$\mathbf{V = \frac{4}{3}\pi P_f^3(r)} \qquad \textbf{(II.5.2)}$$

The number of electrons in spatial coordinates in this phase space gives:

$$\mathbf{n(r) = \frac{8}{3l^3}\pi P_f^3} \qquad \textbf{(II.5.3)}$$

The kinetic energy of the homogeneous gas is given by the following formula:

$$\mathbf{T = \frac{3}{5}\rho} \qquad \textbf{(II.5.4)}$$

A means that the density of kinetic energy is given as follows:

$$\mathbf{E(\rho) = \frac{3}{5} * \frac{\hbar}{2m}(3\pi^2)\rho^{\frac{5}{3}}} \qquad \textbf{(II.5.5)}$$

So the kinetic energy is written in the form

$$\mathbf{T_{TF} = C_K \int \rho\,(r)^{\frac{5}{3}}\,dr} \qquad \textbf{(II.5.6)}$$

With $C_K = 3(3\pi^2)^{2/3}/10 = 2.871\,u.a,$ that is to say, the inhomogeneous system is locally considered as a homogeneous system, which is the same approximation used in density functional theory (DFT).The weak point of this approach lies, however, in the expression of kinetic energy in the absence of orbitals, which does not allow it to achieve satisfactory precision. A little later, Dirac [13] proposed that exchange effects be taken into account by incorporating a term corresponding to the exchange energy density in a homogeneous gas of electrons. All these previous approximations contributed to the development of density functional theory.

II.5.3 The Hohenberg-Kohn theorem:

It was in 1964 that Hohenberg and Kohn [11] established two theorems that form the basis of DFT.

II.5.4 First theorem of Hohenberg and Kohn:

It is stated as follows: "any physical property of a system with N electrons subjected under the effect of a static external potential (Vext) can be expressed, in its ground state, as a functional of the electronic density ρ(r)".

This theorem highlights a unique correspondence between the external potential and the electronic density. Since it fixes the number of electrons, it also uniquely determines the wave function and thereby the electronic properties of the system. Thus, for a given system, the energy is expressed as follows:

$$\boldsymbol{E[\rho(r)] = F_{HK}[\rho(r)] + \int \rho(r)\, V_{ext}(r) d(r)} \qquad \textbf{(II.5.1)}$$

With $F_{HK} = T_e[\rho(r)] + V_{ee}[\rho(r)]$,which is the Hohenberg-Kohn functional containing the kinetic energy and the potential energy due to the electron-electron repulsive interaction.

II.5.5 Second theorem of Hohenberg and Kohn:

The second theorem of Hohenberg and Kohn [11] is a variational principle analogous to the one initially proposed in the Hartree-Fock approach for a functional of the wave function:

$$\boldsymbol{\frac{\partial E(\psi)}{\partial(\psi)} = 0} \qquad \textbf{(II.5.2)}$$

But applied this time to an electronic density functional:

$$\boldsymbol{\left(\frac{\partial E[\rho(\vec{r})]}{\partial \rho(\vec{r})}\right)_{\rho_0(\vec{r})} = 0 \qquad \rho_0(\vec{r})} \qquad \textbf{(II.5.3)}$$

is the electronic density of the ground state.This second theorem states that for any multi-electronic system with a number of electrons N and an external potential V_{ext}.The total energy of the system $E[\rho(\vec{r})]$reaches its minimum value when the density $\rho(\vec{r})$corresponds to the exact density of the ground state $\rho_0(\vec{r})$:

$$\boldsymbol{E(\rho_0) \quad = minE(\rho)} \qquad \textbf{(II.5.4)}$$

The demonstration that the total energy of a system in the ground state is a functional of the electronic density, Hohenberg and Kohn expressed this functional $E[\rho(\vec{r})]$according to the following expression:

$$E[\rho(\vec{r})] = F_{HK}[\rho(\vec{r})] + \int V_{ext}(\vec{r})\rho(\vec{r})d^3\vec{r} \qquad \text{(II.5.5)}$$

In which $V_{ext}(\vec{r})\rho(\vec{r})r$ represents the external potential acting on these particles and $F_{HK}[\rho(\vec{r})]$represents the universal functional of Hohenberg and Kohn.Unfortunately, the Hohenberg-Kohn theorem does not provide any indication of the form of $F_{HK}[\rho(\vec{r})]$There is no exact formulation to express the kinetic energy as a functional of the electronic density.The Kohn-Sham equations [14, 15, 16] present the only solution to this problem, which is established with the aim of providing the necessary foundations to effectively exploit the Hohenberg-Kohn theorems [11].

II.5.5.1 Kohn and Sham theorem

Kohn and Sham had the idea, in 1965, to consider a fictitious system of N independent electrons whose ground state is the Slater determinant formed by N orbitals of electrons, and whose electron density is the same as that of the true interacting electron system.The Schrödinger equation is therefore reformulated in terms of what is commonly referred to as the Kohn-Sham equation [1], which is actually a Schrödinger equation with an effective potential in which quasi-particles move.The Kohn-Sham equations are coupled by the electronic density

$$\rho(r) = \sum_i \psi_i(r) * \psi_i(r) \qquad \text{(II.5.6)}$$

With the coupling included in the solution obtained iteratively.For the expansion of orbitals in terms of a basis of wave functions, different bases can be used.Once this choice is made, the orbitals are used to find a better density \(\rho\) through a self-consistent cycle.Kohn and Sham showed that the true density is given by the self-consistent solution of the set of single-particle Schrödinger-type equations, called the Kohn-Sham equations:

$$-\left\{\frac{1}{2}\Delta^2 + V_{KS}(r)\psi_i(r) = \varepsilon_i\psi_i(r)\right\} \qquad \text{(II.5.7)}$$

$$\rho(r) = \sum_{occup}|\psi_i(r)|^2 \qquad \text{(II.5.8)}$$

$$V_{KS} = V_{ext}(r) + V_H(r) + V_{XC}(r) \qquad \text{(II.5.9)}$$

With:

$V_{XC}(r)$: The exchange-correlation potential given by:

$$V_{XC}(r) = \frac{\partial E_{XC}[\rho(r)]}{\partial \rho(r)} \qquad \text{(II.5.10)}$$

$V_{XC}(r)$**:** Represents the ionic potential

$V_H(r)$**:** Represents the term of Hartree given by:

$$V_H(r) = \int \frac{\rho(\vec{r})}{|\vec{r}-\vec{r}'|} d^3\vec{r} \qquad \text{(II.5.11)}$$

The total energy is determined through the solution of the Kohn–Sham equations, as expressed by the following formalism :

$$E(\rho) = \varepsilon_i - \int \frac{\rho(r)\rho(r')}{|r-r'|} dr\, dr' + E_{XC}(\rho) - \int V_{XC}(r)\rho(r) dr \qquad \text{(II.5.12)}$$

The solution of the Schrödinger equation within the framework of the Kohn–Sham approximation is reduced to solving an equation of the following form:

$$H_{k-s} = \frac{-\hbar^2 \nabla_i^2}{2m} + \frac{e^2}{4\pi\varepsilon_0} \int \frac{\rho(\vec{r}')}{|\vec{r}-\vec{r}'|} dr' + V_{xc} + V_{ext} \qquad \text{(II.5.13)}$$

The Schrödinger equation is obtained as follows :

$$|H_{kS}\Psi_i| = |E_i\Psi_i| \qquad \text{(II.5.13)}$$

The various methods used to calculate electronic structure based on Density Functional Theory (DFT) can be categorized according to the representations employed for the electron density, the potential, and the Kohn–Sham orbitals. These orbitals are described by the following:

$$\Psi_i(\vec{k},\vec{r}) = \sum C_{ij} \emptyset_j(\vec{k},\vec{r}) \qquad \text{(II.5.14)}$$

$\emptyset_j(\vec{k},\vec{r})$**:** are the basis functions

C_{ij} **:** The coefficients of the basis function expansion.

II.5.5.2 Self-consistent field (SCF) approach in the calculations

Solving the Kohn–Sham equations at high-symmetry points in the first Brillouin zone helps simplify the calculations. These equations are solved iteratively using a self-consistent iteration cycle, as illustrated in the flowchart in **(Fig.II.1).** The process begins with an initial trial density ρ_{in} for the first iteration. Typically, a superposition of atomic densities is used. Then, the Kohn–Sham (K-S) matrix is constructed, and by solving the equations for the expansion coefficients, the Kohn–Sham orbitals are obtained. At this stage, a new density ρ_{out} is computed. If the density or energy has significantly changed (based on a convergence criterion), the cycle returns to the first step. The input and output charge densities ρ_{in} and ρ_{out} are then mixed as follows[2]:

$$\rho_{in}^{i+1} = (1-\alpha)\rho_{in}^{i} + \alpha\rho_{out}^{i} \tag{II.5.15}$$

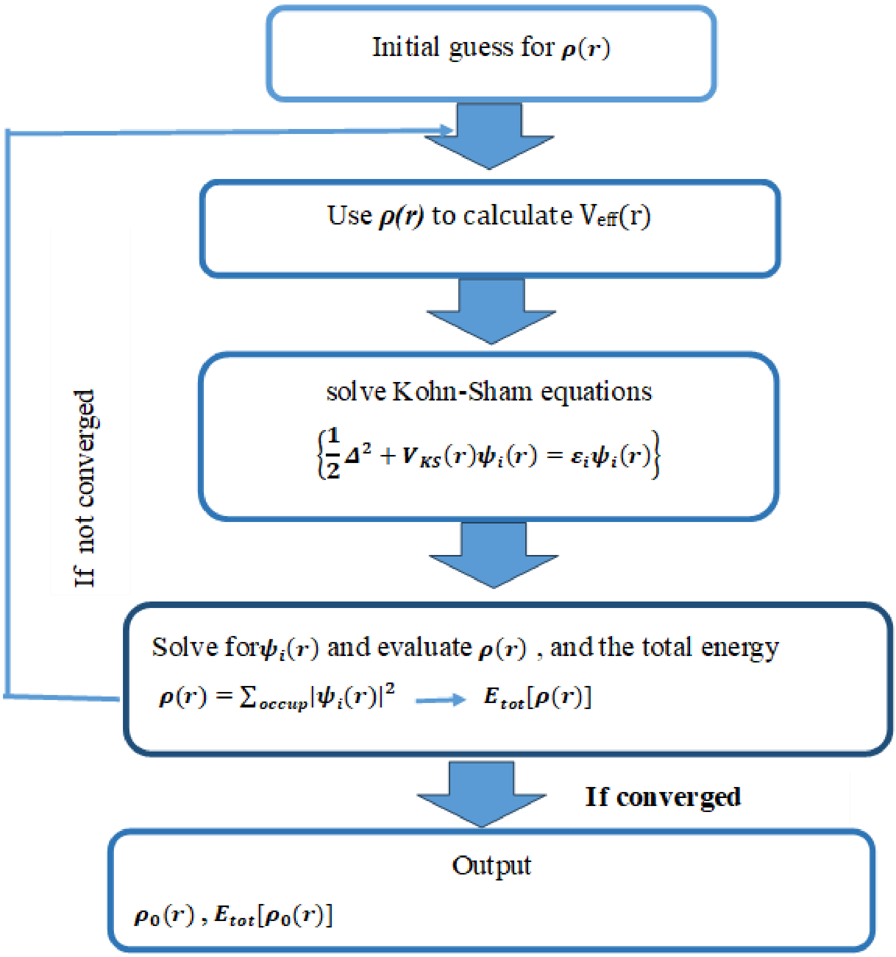

Fig.II.1 :**Self-consistent iterative process used to solve the Kohn-Sham equations**

II.5.5.3 The exchange-correlation functional

To address the limitations of DFT in accurately describing the exchange-correlation term, the approximations used for defining the exchange-correlation functional must be sufficiently general to apply across a wide range of systems. The interactions between electrons give rise to three main types of effects: exchange, dynamic correlation, and non-dynamic correlation.

II.5.5.4 The Local Density Approximation (LDA)

The local density approximation LDA is the approximation on which practically all currently employed approaches are based employed. It was first proposed by Kohn and Sham; the philosophy of this approximation was already present in the works of Thomas and Fermi.this approximation constitutes the simplest approach to express exchange and correlation energy.It states that the electronic density of an inhomogeneous electron gas is locally identical to that of a uniform (homogeneous) electron gas of the same density[3] [4] . exchange and correlation energy exactly known:

$$\boldsymbol{E_{XC}{}^{LDA}[\rho] = \int \rho(\vec{r})\varepsilon_{XC}{}^{LDA}[\rho(\vec{r})]\, d^3\,\vec{r}} \qquad \textbf{(II.5.16)}$$

In which $E_{XC}{}^{LDA}[\rho(\vec{r})]$ represents the exchange-correlation energy for every electron in a system of mutually interacting electrons with uniform density $\rho(\vec{r})$. The corresponding exchange-correlation potential is:

$$\boldsymbol{V_{XC}{}^{LDA} = \frac{\delta\rho(\vec{r})\varepsilon_{XC}{}^{LDA}[\rho(\vec{r})]}{\delta\rho(\vec{r})}} \qquad \textbf{(II.5.17)}$$

The function$E_{XC}{}^{LDA}[\rho]$ can be separated into an exchange term and a correlation term as follows:

$$\boldsymbol{E_{XC}{}^{LDA}[\rho] = \varepsilon_X{}^{LDA}[\rho] + \varepsilon_C{}^{LDA}[\rho]} \qquad \textbf{(II.5.18)}$$

There are other parameterizations for the correlation energy of a homogeneous electron gas, including those by Kohn and Sham, Hedin and Lundqvist[5], , and Perdew and Wang .

It should be noted that in the case of spin, within the LDA/LSDA framework (LSDA: Local Spin Density Approximation), leads to the following expression [6].

$$\boldsymbol{E_{XC}{}^{LDA}[\rho\uparrow(\vec{r}),\rho\downarrow(\vec{r})] = \int \rho(\vec{r})\,\varepsilon_{XC}{}^{LDA}[\rho\uparrow(\vec{r}),\rho\downarrow(\vec{r})]\, d^3\,\vec{r}} \qquad \textbf{(II.5.19)}$$

II.5.5.5 The Generalized Gradient Approximation (GGA)

The Generalized Gradient Approximation (GGA) [7,8], sometimes also referred to as non-local methods, was developed to account for the variation in electron density by expressing the exchange and correlation energies as functions not only of the density itself but also of its gradient (i.e., its first derivative |∇ρ(r)|). This allows for consideration of the inhomogeneity of the electron gas density [9]. In general, within the GGA framework, the exchange-correlation energy is defined as follows:

$$\boldsymbol{E_{XC}{}^{GGA}[\rho(\vec{r})] = \int \rho(\vec{r})\varepsilon_{XC}{}^{GGA}[\rho(\vec{r})|\nabla\rho(\vec{r})|]\, d^3\,\vec{r}} \qquad \textbf{(II.5.20)}$$

Compared to LDA, the Generalized Gradient Approximation (GGA) provides enhanced accuracy in describing chemical bonding characteristics, such as bond lengths, bond angles, and binding energies. Several forms of GGA have been proposed, including GGA-PBE and GGA-WC

II.5.5.6 Generalized Gradient Approximation – Perdew–Burke–Ernzerhof (GGA-PBE)

A simple formulation of a generalized gradient approximation for the exchange-correlation energy of electrons was proposed by Perdew, Burke, and Ernzerhof (PBE). This approximation provides a correct linear response of the uniform electron gas, but its numerical performance remains limited, leading to errors in the prediction of thermochemical data for molecular systems as well as atomic energies [10].

II.5.5.7 eneralized Gradient Approximation – Wu–Cohen

A more recent development by Z. Wu and R.E. Cohen (WC) [11] introduced a new generalized gradient approximation (GGA) for the exchange energy functional. This formulation significantly enhances the accuracy of structural parameter calculations in solids. Moreover, it is computationally efficient and free of any empirical fitting parameters .

II.5.5.8 modified Becke–Johnson potential (mBJ Approximation)

He functional developed by Tran and Blaha [29], referred to as (mBJ), is a modified version of the Becke–Johnson functional. This latter has quickly demonstrated its effectiveness compared to the most commonly used calculation methods, such as LDA [13] and GGA [30]. In their article published on June 3, 2009, in *Physical Review Letters*, Tran and Blaha proposed a modified version of the Becke–Johnson functional [31], presented in the following form:

$$\boldsymbol{V_{x\sigma}}^{\boldsymbol{mbj}} = \boldsymbol{\upsilon^{\mathrm{mBJ}}_{\mathrm{x};\sigma}(\mathrm{r}) = \mathrm{c}\upsilon^{\mathrm{BR}}_{\mathrm{x};\sigma}(\mathrm{r}) + (3\mathrm{c}-2)\frac{1}{\pi}\sqrt{\frac{5}{12}}\sqrt{\frac{2\mathrm{t}_\sigma(\mathrm{r})}{\rho_\sigma(\mathrm{r})}}} \qquad (\mathbf{II.5.21})$$

With:

$\boldsymbol{\rho(r)\sum_{i=1}^{N\sigma}|\psi_{i.\sigma}(r)|^2}$:The electron density.

$\boldsymbol{t_\sigma(r) = \frac{1}{2}\sum_{i=1}^{N\sigma}|\psi_{i.\sigma}(r)\nabla\psi_{i.\sigma}(r)|^2}$:The kinetic energy density.

$\boldsymbol{V_{x\sigma}}^{\boldsymbol{mbj}}$:The Becke–Roussel potential .

The main modification lies in the introduction of a parameter in the functional's formula. It is worth noting that C = 1 if this parameter is set to a specific value, the original Becke–Johnson functional

[13] is recovered. This parameter was chosen to depend linearly on the square root of $\frac{|\nabla\rho(r)|}{\rho(r)}$ the average of a certain quantity. The proposed form for **c** is as follows:

$$\boldsymbol{C = \alpha + \beta\left[\frac{1}{V_{Cell}}\int_{cell}\frac{|\nabla\rho(r)|}{\rho(r')}d^3\,r'\right]^{\frac{1}{2}}} \qquad \textbf{(II.5.22)}$$

α and β are two free parameters, V_{Cell} the volume of the unit cell of the system.

II.5.5.9 The Augmented Plane Wave (APW) method

The development of the APW method is based on Slater's observation [14] that:

- Near the nuclei, the potential and wave functions are similar to those of an atom; they vary strongly but according to spherical symmetry.
- Between the atoms, the potential and wave functions are smooth.

Therefore, the space can be divided into two regions: (1) spheres called (muffin-tin) encompassing the atoms and (2) an interstitial region delineating the residual space not occupied by the spheres **(Fig.II.2),** in which two appropriate categories of basis are used:

1. Radial functions multiplied by spherical harmonics in the atomic (muffin-tin) spheres.

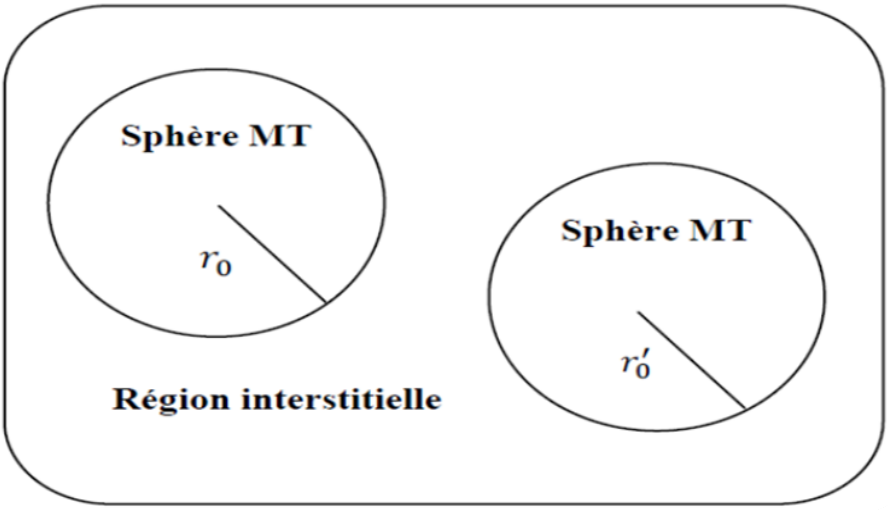

Figure II.2. Diagram of the distribution of the unit cell into atomic spheres and interstitial region

Thus, the wave function $\phi(\vec{r})$ is then of the form:

$$\begin{cases}\displaystyle\sum_{\mathbf{lm}}\mathbf{A_{lm}U_l(r)Y_{lm}(r)} & \mathbf{r < r_0}\\ \displaystyle\frac{\mathbf{1}}{\sqrt{\boldsymbol{\Omega}}}\sum_{\mathbf{G}}\mathbf{C_G\,e^{i(\vec{K}+\vec{G})\vec{r}}} & \mathbf{r > r_0}\end{cases} \qquad \textbf{(II.5.23)}$$

Where Ω is the volume of the cell, C_G and A_{lm} are the expansion coefficients, and$U_l(r)$ is the regular solution of the Schrödinger equation for the radial part given by : [15]

$$\left(-\frac{d^2}{dr^2}+\frac{l(l+1)}{r^2}+V(r)-E_l\right)rU_l(r) \;=0 \qquad (II.5.24)$$

V(r): represents the spherical potential, and E_l is the linearization energy.

The center of the sphere is taken as the origin, and the coefficients A_{lm} are calculated based on the plane wave coefficients **C**GC and the energy parameters E_l which serve as variational parameters in the APW method. To ensure continuity of the wave function at the boundary of the Muffin-Tin sphere, the plane wave is expanded in terms of spherical Bessel functions, leading to the following result[15] :

$$A_{lm}=\frac{4\pi i^l}{\sqrt{\Omega}U_l(r_l)}\sum_G C_G\,J_l\,(|K+G|r_0)Y^*_{lm}(K+G) \qquad (II.5.25)$$

J_l: The Bessel function of order 1.

CGC: The coefficients of the plane waves present in the interstitial region.

II.5.5.10 The Full-Potential Linearized Augmented Plane Wave (FP-LAPW) method

In this method, the basis functions inside the sphere are linear combinations of the radial functions$U_l(r)Y_{lm}$ and their derivatives $\dot{U}_l(r)Y_{lm}(r)$with respect to energy. The functions are defined as in the APW method, and the function$U_l(r)$ must satisfy the following condition:

$$\left(-\frac{d^2}{dr^2}+\frac{l(l+1)}{r^2}+V(r)\;-E_l\right)r\dot{U}_l(r)=rU_l(r) \qquad (II.5.26)$$

The wave function is written as follows:

$$\phi(\vec{r})=\begin{cases}\sum_{lm}\left[A_{lm}U_l(r)+B_{lm}\dot{U}_l(r)\right]Y_{lm}(r) & r<r_0\\ \frac{1}{\sqrt{\Omega}}\sum_G C_G\,e^{i(\vec{K}+\vec{G})\vec{r}} & r>r_0\end{cases} \qquad (II.5.27)$$

A_{lm}: are coefficients corresponding to the function $U_l(r)$.

B_{lm} : are coefficients corresponding to the function$\dot{U}_l(r)$.

In the FP-LAPW method, the basis functions behave as plane waves exclusively within the interstitial regions similar to the APW approach .Near the linearization energy E_l , the radial functions can be approximated through the following expansion : [16]

$$\mathbf{U_l(E, r) = U_l(E_l, r) + (E - E_l)\,\dot{U}_l(E_l, r) + O((E - E_l)^2)} \qquad \mathbf{(II.5.28)}$$

With $O((E - E_l)^{2})$ denotes the quadratic error made

The (FP-LAPW) method introduces an error in the wave functions of the order of $O((E - E_l)^{2}$, and another in the band energy of the order of $O(E - E_l)^{4}$ [8]. All valence bands within a wide energy range can be obtained through a single calculation E_L . In case this is not possible, the energy window is divided into two parts.

1. Hohenberg, P and Kohn, W. (1964). Phys. Rev. B **136**, 864.
2. Frayret, C. ‘2004). Thèse de doctorat, Université de Bordeaux I.
3. Schwarz, K and Blaha, P. (1996).Lecture Notes in Chemistry 67,139.
4. Dreizler, R and da Provincia, J. (1985). Density Functional Methods in Physics (Plenum, NewYork.
5. Carisson, A *et al,.* (1985). Phys. Rev. B 32 1386.
6. Bacewicz, R and Ciszek, T. (1988). Appl. Phys. lett. 52 1150.
7. Skriver, H. (1982). Phys. Rev. Lett. 49, 1768.
8. Chadi, D. (1979). Phys. Rev. B 19, 2074.
9. Perdew, J *et al,.* (1996). *“Generalized Gradient Approximation Made Simple”*. Phys. Rev. Lett., 77, 3865.
10. Becke, A and Johnson, E. (2006). *“Simple effective potential for exchange”*, Chem. Phys., 124, 221101.
11. Wu, Z and Cohen, R. (2006). Phys. Rev. B73, 235116.
12. Tran, F and Blaha, P. (2009). Phys. Rev. Lett. 102-226401.
13. Becke, A and Johnson, J. (2006). Chem. Phys. 124 -221101.
14. Slater, J. (1937). Phys. Rev. 51, 846.
15. Matheiss, L and Hamann, D. (1986). Phys.Rev.B33, 823.
16. Koelling, D and Arbman, D. (1975). Phys. F 5, 2041.

Chapter 3: Simulation Results and Analysis of Structural, Electronic, and Optical Properties

III.1 Introduction

Crystalline-structured materials play a significant role in the development of modern technology, where the primary focus is on materials that exhibit half-metallic properties to exploit electron spin for information storage and processing. This chapter focuses on studying the electronic, and optical properties of the double perovskite Ba_2BBiO_6 (where B is Sm or Tb) using density functional theory (DFT) with precise computational techniques such as the FP-LAPW method and mBJ-GGA functionals. The study covers the crystal structure, electronic bandgap, electronic density of states (DOS), as well as optical properties such as the absorption coefficient and optical conductivity. The results show that the Ba_2SmBiO_6 compound exhibits spin-dependent half-metallic behavior, making it a promising candidate for spintronic applications, while Ba_2TbBiO_6 behaves more like a direct bandgap semiconductor, suitable for energy and photodetection applications. This study aims to provide a comprehensive understanding of the properties of these two compounds and their potential use in future devices.

III.2 Crystal structure

Following the detailed introduction aimed at contextualizing the reader and outlining the search for half-metallic materials for spintronic applications based on Density Functional Theory (DFT), our focus turned to double perovskite oxides with the general formula $A_2BB'O_6$, owing to their remarkable physical properties.

In this study, we specifically investigated the cubic double perovskites Ba_2BBiO_6 with B is Sm or Tb .

At ambient pressure, the compound crystallizes in a cubic crystal system with space group Fm-3m. The unit cell is characterized by equal lattice parameters, with $a = b = c$ approximately 8.65 Å[1]. The unit cell contains four formula units (Z = 4), reflecting the symmetry and packing efficiency of the cubic perovskite structure.

Within this structure, the atomic positions are well-defined: barium (Ba) atoms occupy the 8c Wyckoff positions at (0.25, 0.25, 0.25), samarium (Sm) is located at the 4a site (0, 0, 0), and bismuth (Bi) occupies the 4b site at (0.5, 0.5, 0.5). Oxygen atoms are situated at general positions of the form (x, 0, 0), where the parameter x reflects possible distortions in the BO_6 octahedra, which can influence the compound’s electronic and structural properties.

The cubic structure of Ba_2BBiO_6 used in this study is illustrated in Figure.1. The crystallographic visualization of this cubic structure was obtained using the 3D visualization program

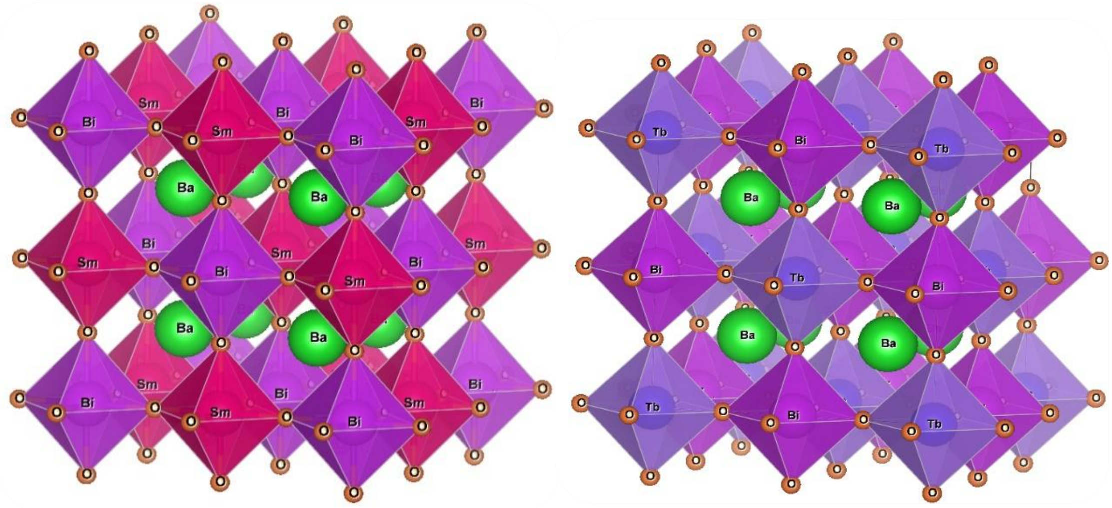

(a) **(b)**

Figure III.1. Schematic crystal structure of Ba_2BBiO_6 (B= Sm, Tb)

The electronic configuration of each element used is as follows:

Ba: [Xe] $6s^2$ **Bi :** [Xe] $4f^{14}\ 5d^{10}\ 6s^2\ 6p^3$ **O:** $1s^2\ 2s^2\ 2p^4$

Sm: [Xe] $4f^6\ 6s^2$ **Tb:** [Xe] $4f^9\ 6s^2$

The calculations were carried out using the Wien2k code [2], which is an implementation of the full-potential linearized augmented plane wave (FP-LAPW) method. The exchange-correlation potential was treated using the generalized gradient approximation (GGA) [3] and the GGA+U approach. However, for calculating the electronic properties, we additionally used the modified Becke–Johnson (mBJ) potential developed by Tran and Blaha .

The rationale behind using both GGA+U and mBJ+GGA methods lies in the fact that the former accurately describes electron correlation in transition metals, while the latter provides energy band gap values. This allows us to improve the results in terms of both magnetic moments and band gaps of the studied compounds.

In the FP-LAPW method, space is divided into non-overlapping Muffin-Tin (MT) spheres and an interstitial region between them. The plane waves are limited by the condition $RMT \cdot Kmax = 9$, where RMT is the smallest MT radius and Kmax is the maximum magnitude of the wave vector K.

For the sampling of the first Brillouin zone in reciprocal space, a k-point grid of 1000 pointsequivalent to a (10×10×10) mesh—was found sufficient to ensure convergence of the total energy.

The chosen Muffin-Tin radii (RMT) for Ba, Sm, , Bi, and O atoms were respectively 2.50, 2.24 ,2.30 and1.83 . for the compound Ba_2TbBiO_6 The chosen Muffin-Tin radii (RMT) for atoms were respectively 2.50, 2.27, 2.25, 1.84 .

III.3 The structural properties of the compound

The determination of structural properties is the first essential step that precedes the calculation of a material's physical properties from its microscopic structure. To perform these calculations, the initial task involves determining the lattice parameter. Clearly, the choice is limited to two options: either the value obtained from experiment or the one calculated by minimizing the total energy of the system's unit cell—referred to as the theoretical value.

Nowadays, it is possible to compute the total energy of solids with reasonable accuracy by applying certain approximations such as the Generalized Gradient Approximation (GGA) and the Local Density Approximation (LDA) [4].

Using the Wien2k code [2], we performed a self-consistent total energy calculation for several values of the lattice parameter a taken around the experimental value. To determine the equilibrium parameters such as the lattice constant (a_0), the bulk modulus, and its derivative, the total energy was calculated as a function of volume. The resulting curve was then fitted using the Murnaghan equation of state [5], given by the following expression:

$$\mathbf{E(V) = E_0 + \frac{B}{B'(B'+1)}\left[V\left(\frac{V_0}{V}\right)^{B'} - V_0\right] + \frac{B}{B'}(V - V_0)} \qquad \mathbf{(III.2.1)}$$

Where E, V, *B'* and B represent, respectively: the total energy, the equilibrium volume, the bulk modulus, and its pressure derivative. The bulk modulus is given by the following formula:

$$\mathbf{B = V\frac{\partial^2 E}{\partial V^2}} \qquad \mathbf{(III.2.2)}$$

And the pressure derivative of the bulk modulus B′:

$$\mathbf{B' = \frac{\partial B}{\partial P}} \qquad \mathbf{(III.2.3)}$$

This study aims to determine the unit cell volume at equilibrium, which allows the extraction of the corresponding lattice constant at the minimum total energy. Furthermore, the bulk modulus and its first pressure derivative are calculated **(Fig.III.2.a et III.2.b)** illustrate the variation of the total energy with respect to the unit cell volume for the Ba_2BBiO_6 compound, using both GGA approximation. The lattice constant is identified at the equilibrium point corresponding to the minimum of the energy curve.

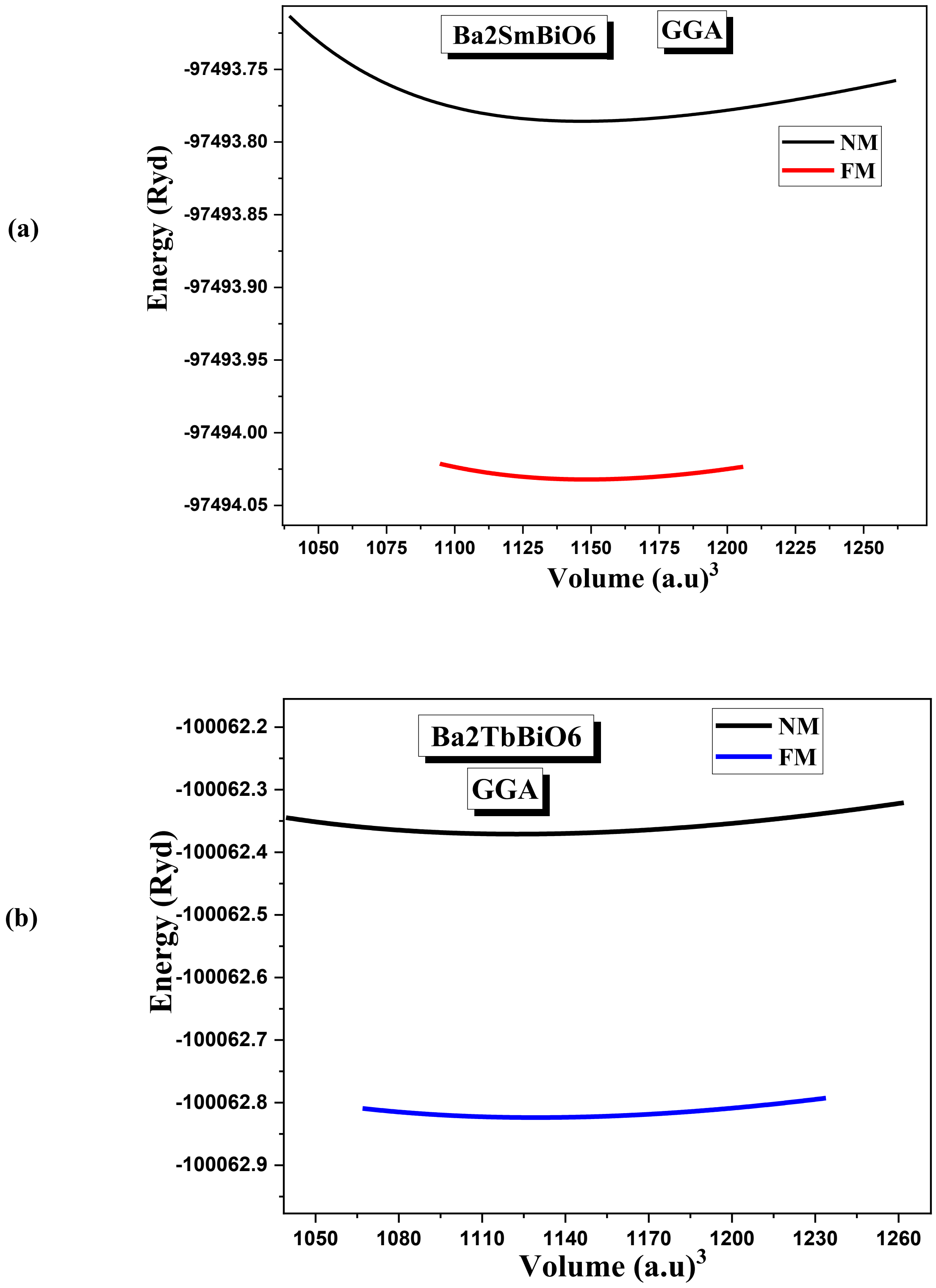

Figure III.2. The calculated energy vs. volume curves for optimizing of Ba_2BBiO_6 (B= Sm, Tb) using GGA approximation for Magnetic and non-magnetic phases.

The energy vs. volume curves were studied using GGA for both magnetic and non-magnetic states. The curves show:

- The magnetic state is more energetically stable, indicating that the structure favors a magnetic ground state.
- A slight difference in optimal volume between Sm and Tb, likely due to their ionic radius difference.

Table 2 presents the calculated structural parameters of Ba_2SmBiO_6 and Ba_2TbBiO_6 in both non-magnetic (NM) and ferromagnetic (FM) states. A comparison between the two magnetic configurations reveals that the FM state is energetically more favorable for both compounds, as indicated by the lower total energy values (E_0). Specifically, Ba_2SmBiO_6 exhibits a slight expansion in lattice constant from 8.7945 Å in the NM state to 8.7967 Å in the FM state, accompanied by a reduction in the bulk modulus B from 124.49 GPa to 106.57 GPa. This suggests increased lattice flexibility when the material adopts a magnetic ordering. Similarly, Ba_2TbBiO_6 also shows a more stable FM phase, with a lower energy minimum and a marginal increase in from 8.7300 Å (NM) to 8.7474 Å (FM). However, in contrast to the Sm-based compound, Ba_2TbBiO_6 exhibits an increase in bulk modulus under FM ordering, indicating enhanced stiffness. The pressure derivative of the bulk modulus (B_P) also varies notably between states, reflecting differences in compressibility behavior under external pressure. These results collectively confirm that magnetic ordering plays a crucial role in stabilizing the structure and modulating mechanical properties in Ba_2BBiO_6 compounds.

Table III.2 the calculated structural parameters of Ba_2SmBiO_6 and Ba_2TbBiO_6 in both non-magnetic (NM) and ferromagnetic (FM) states.

		a_0 (Ang)	B (GPa)	BP	E_0 (Ry)
Ba_2SmBiO_6	**NM**	8.7945	124.4948	14.5017	-97493.786056
	FM	8.7967 8.80[6] 7.48[7]	106.5747 109.94[6]	9.4585 4.23[6]	-97494.032160 -97494.06[6]
Ba_2TbBiO_6	**NM**	8.730	107.5036	5.0182	-100062.370945

	FM	8.7474 8.74[6]	111.9611 114.57[6]	4.8464 4.65[6]	-100062.823780 -100062.82[6]

III.4 Energy Band Structure

The energy band is defined (in solid-state energy regions) as the energy range that allows (or facilitates) electrons to move from the top of the valence band to the bottom of the conduction band. It has been scientifically proven that these bands are not fixed in electronic states and do not remain static for the electrons that occupy them at a given time. Energy bands allow electrons to move within the band itself without changing the energy level. In contrast, the forbidden band is the energy gap that separates the energy levels and determines the validity of the material for manufacturing new electronic devices such as solar cells, transistors, integrated circuits, etc.

The first region is also known as the Brillouin Zone, which is the area with the lowest energy in the primary region and is important in studying the properties of crystalline solids. It is a part of the first Brillouin zone in this study. It should be noted that the study of the effect of the body structure on this region can be done using the representation shown in **(Fig.III.3)**, which shows the first Brillouin zone structure for a face-centered cubic lattice (FCC).

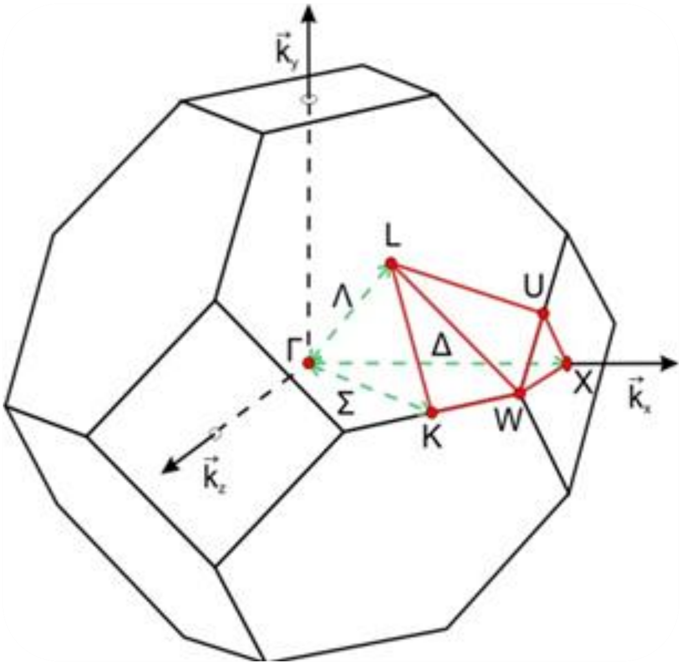

Figure III.3. The first Brillouin zone of FCC structures.

To determine the band structure of the compound, we used Density Functional Theory (DFT) and the approximations GGA-mBJ, which are among the best approaches used in structural and electronic studies. The curves shows the bands structure of Ba_2BBiO_6 calculated using the approximations GGA-mBJ .

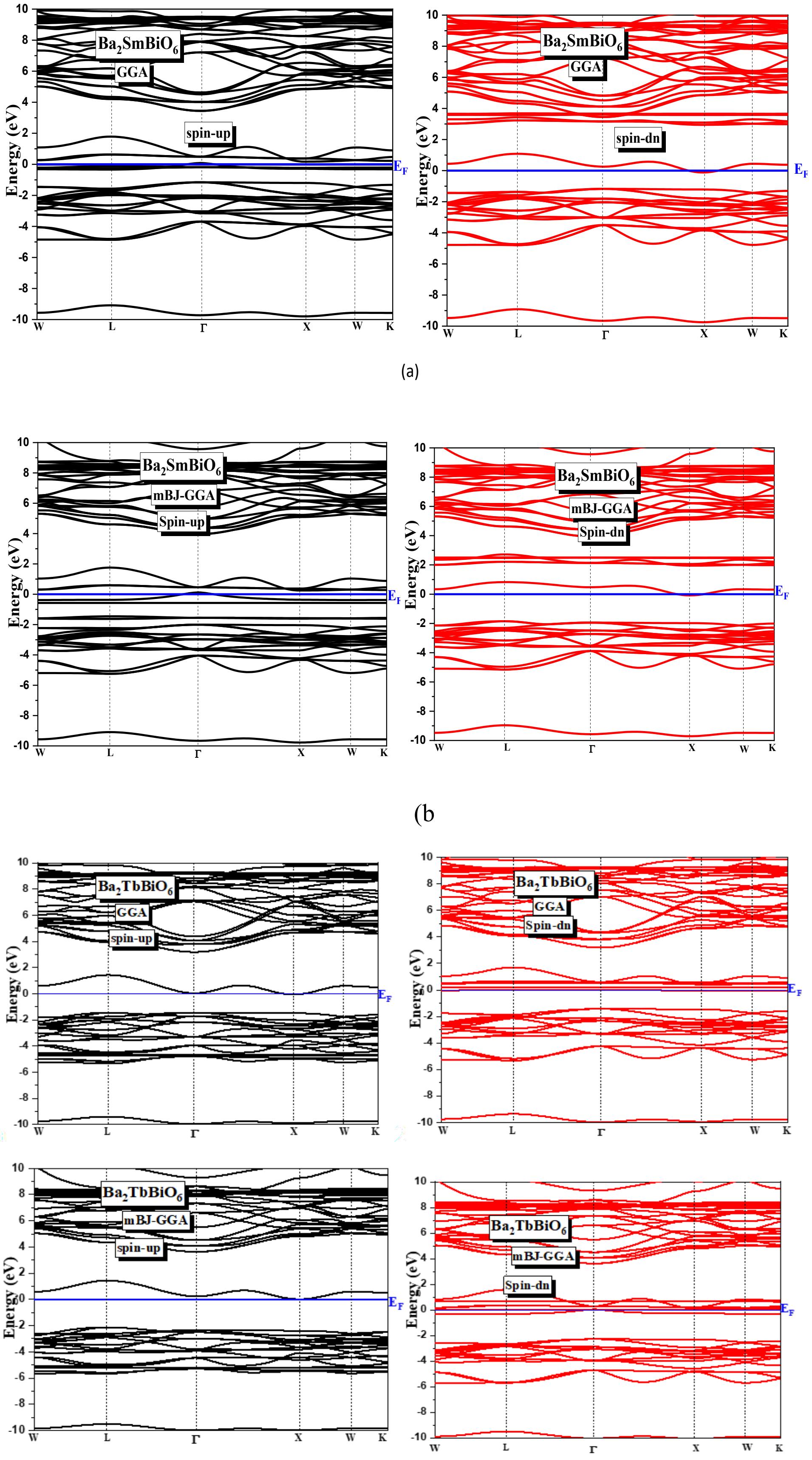

(a)

(b

Figure III.4. The band structures for spin (up) and spin (dn) configurations of Ba$_2$SmBiO$_6$ and Ba$_2$TbBiO$_6$ (a) using GGA and (b) with mBJ-GGA

The numerical values presented in the table provide a detailed comparison of the band gaps for the compounds Ba_2SnBiO_6 and Ba_2TbBiO_6 using both GGA and mBJ methods, categorized by spin orientation (Spin-up and Spin-down). By analyzing the band structure diagrams for Ba_2TbBiO_6, a clear consistency can be observed between the numerical results and the visual representation of the electronic bands. For instance, the GGA Spin-up diagram shows a distinct band gap near the Fermi level, which corresponds to the calculated value of 2.21 eV listed in the table. In contrast, the Spin-down state shows overlapping between the valence and conduction bands, indicating metallic behavior, which is also reflected in the table. When using the mBJ method, a noticeable widening of the band gap is observed for the Spin-up state, reaching 3.07 eV, again confirmed by the band diagrams, while the Spin-down state remains metallic. For Ba_2SmBiO_6, , the table indicates metallic behavior for Spin-up and a finite band gap for Spin-down, suggesting spin-polarized behavior. These results highlight the importance of combining visual band structure analysis with numerical data to better understand the electronic properties of the studied compounds and demonstrate the improved accuracy of the mBJ functional in estimating band gaps compared to GGA.

Table III.3. The band gap of Ba_2BBiO_6 (B=Sm, Tb) using GGA, and mBJ.

	GGA		**mBJ**	
	Spin up	Spin dn	Spin up	Spin dn
Ba_2SmBiO_6	metal	1.74	metal	2.34
Ba_2TbBiO_6	2.21	metal	3.07	metal

III.5 Electronic Density of States (DOS)

The electronic density of states (DOS) is one of the most interesting electronic properties in the field of materials physics. In fact, DOS calculations allow us to determine the general distribution of states as a function of energy, to understand the nature of states and the bonds responsible for them, and the type of orbital character prevailing in each region to comprehend the structure of the electronic domain. It also enables us to determine the energy gap value for semiconductors.

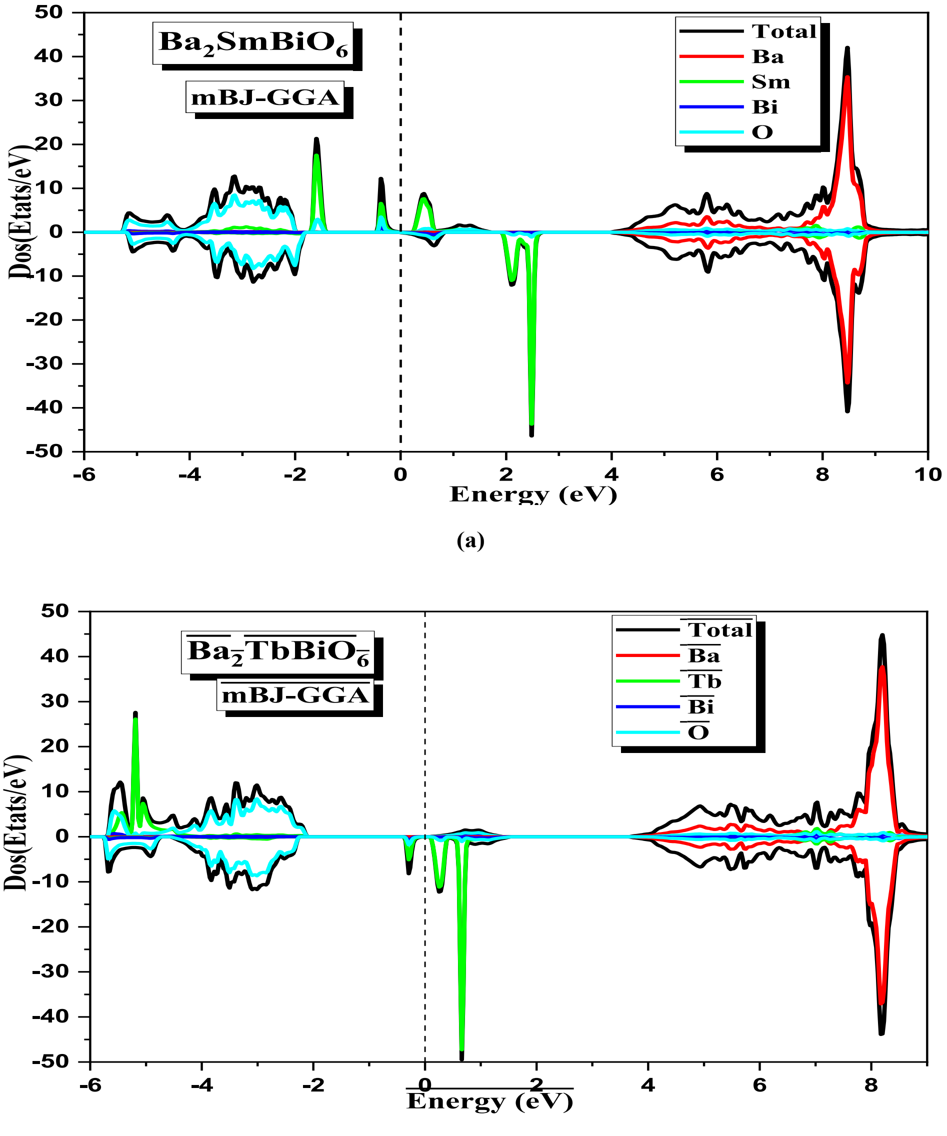

Figure III.5. Density of states for spin (up) and spin (dn) configuration of (a) Ba_2SmBiO_6 (b) Ba_2TbBiO_6 using mBJ-GGA

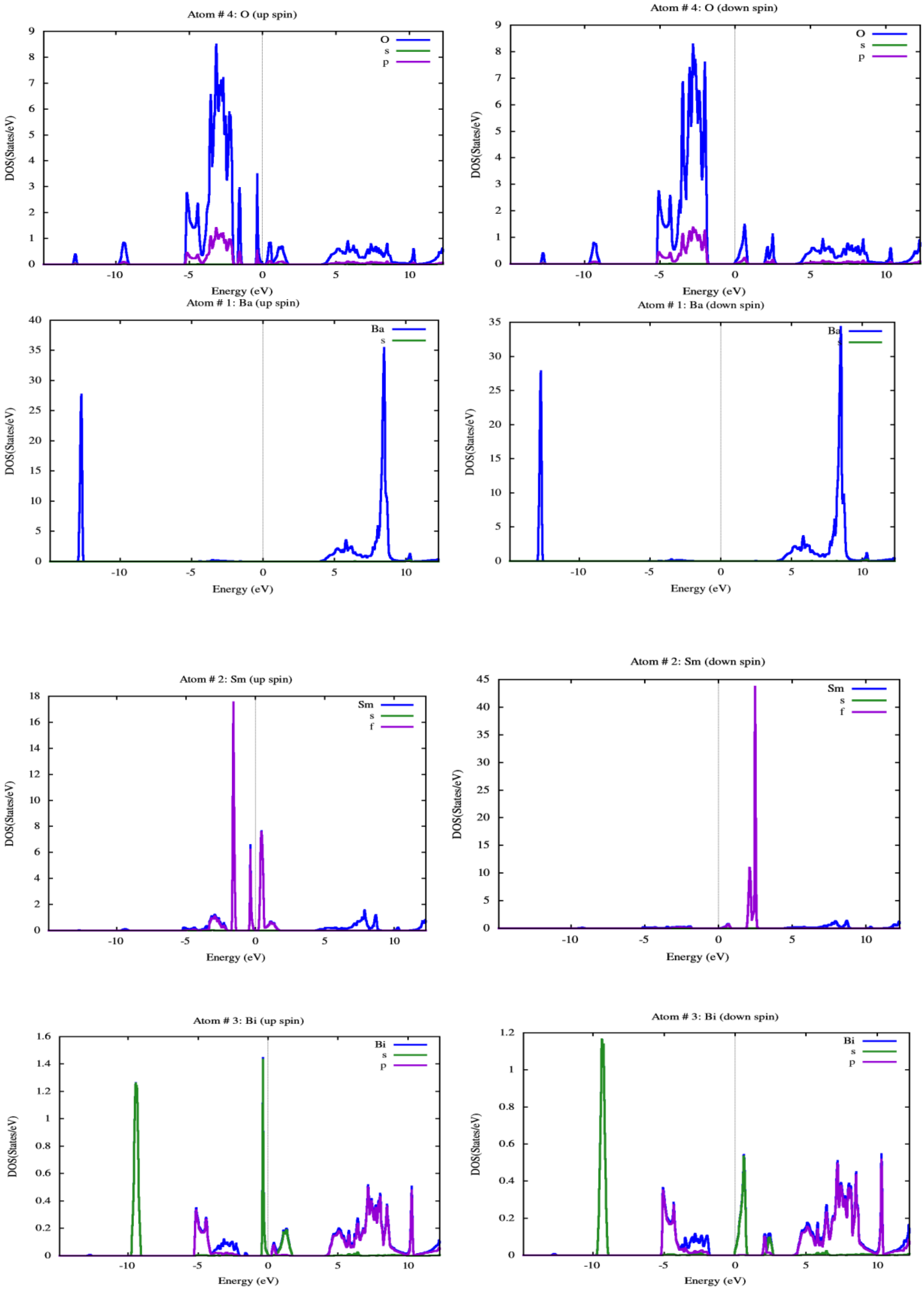

Figure III.6.Partial density of states pdos for spin (up) and spin (dn) configuration of (a) Ba_2SmBiO_6 (b) Ba_2TbBiO_6 using mBJ-GGA

Fig (a): based on the density of states (DOS) analysis of Ba_2SmBiO_6, the elemental contributions to the electronic structure were identified by evaluating the intensity of the projected DOS curves near the Fermi level. In the valence band region (below 0 eV), samarium (Sm) and oxygen (O) exhibit the most significant contributions, with Sm displaying sharp and intense peaks, indicating a strong localization of electronic states. In contrast, the conduction band (above 0 eV) shows dominant contributions from barium (Ba). Notably, Sm contributes prominently near the Fermi level, suggesting its major role in shaping the electronic behavior of the compound, especially in defining the band gap characteristics. This highlights Sm as the most electronically active species in the vicinity of the band edges, influencing both the density of states and potential electronic transitions.

Based on the projected density of states (PDOS) **(Fig.III.6)** analysis for the Sm atom, it is evident that the f orbital exhibits the most significant contribution to the electronic structure. Both the spin-up and spin-down graphs show pronounced peaks in the f orbital near the Fermi level (0 eV), indicating strong involvement in the valence and conduction band edges. In contrast, the s and p orbitals contribute minimally. The dominance of the f orbital, particularly around the band gap region, suggests that it plays a crucial role in determining the electronic and optical properties of the compound.

For Ba2TbBiO6 illustrated in **(Fig.III.5.b)** the analysis of the total density of states (DOS) for reveals the presence of a clear energy gap between the valence band and the conduction band, indicating that the compound behaves as a semiconductor. The top of the valence band is located just below the Fermi level (0 eV), while the conduction band starts just above it, suggesting a direct or nearly direct bandgap.

- **Oxygen (O):** atoms show strong peaks in the valence band, mainly from 2p orbitals. This indicates their key role in bonding.
- **Terbium (Tb):** contributes with sharp 4f peaks near the Fermi level. These states are very localized and do not show clear spin splitting, which means the material is non-magnetic.
- **Bismuth (Bi):** contributes in both the valence and conduction bands, especially through 6s and 6p orbitals, showing it plays an important role in both bonding and conduction.
- **Barium (Ba):** contributes mainly at higher energy levels (above ~5 eV), showing its ionic character without much influence on chemical bonding.

In summary, is a semiconductor, where the electronic properties are mainly governed by the interaction between O (2p) and Bi (6p) orbitals, and the localized nature of Tb (4f) electrons. This makes it a good candidate for applications in electronic and optoelectronic devices.

The projected density of states (PDOS) analysis of shows that the Oxygen 2p orbitals dominate the top of the valence band, while the Bismuth 6p orbitals mainly contribute to the bottom of the conduction band. This overlap suggests the presence of p–p hybridization between Bi and O atoms, which plays an important role in the compound's electronic structure.

The Terbium 4f states appear as sharp and narrow peaks close to the Fermi level, indicating highly localized electrons. These 4f levels do not show a significant difference between spin-up and spin-down states, meaning the material is non-magnetic.

Barium contributes at higher energy levels, mostly above 5 eV, with minimal effect on the bonding or conduction properties. This suggests that Ba acts mainly as a charge donor with an ionic character.

In conclusion, the compound exhibits semiconductor behavior with a clear energy gap and non-magnetic character. Its electronic properties are mainly influenced by the O(2p) – Bi(6p) hybridization and the localized nature of Tb(4f) states, making it a potential candidate for future applications in energy and electronic technologies.

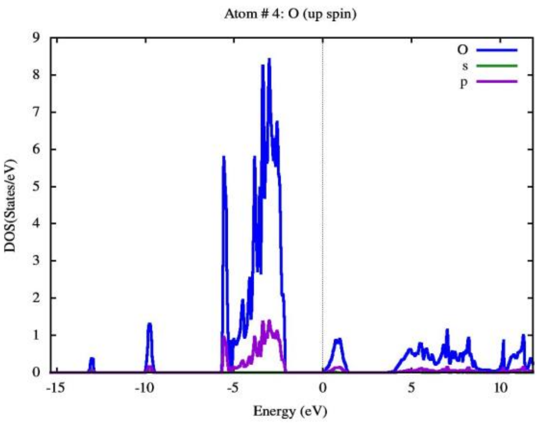

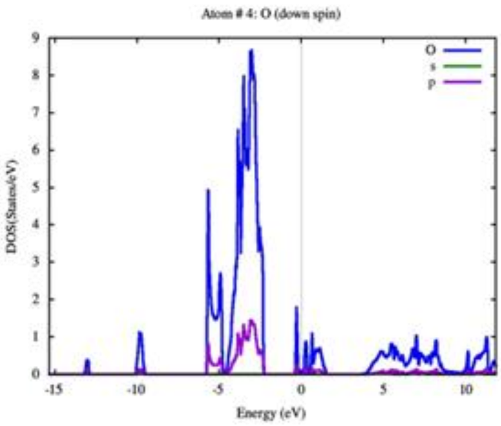

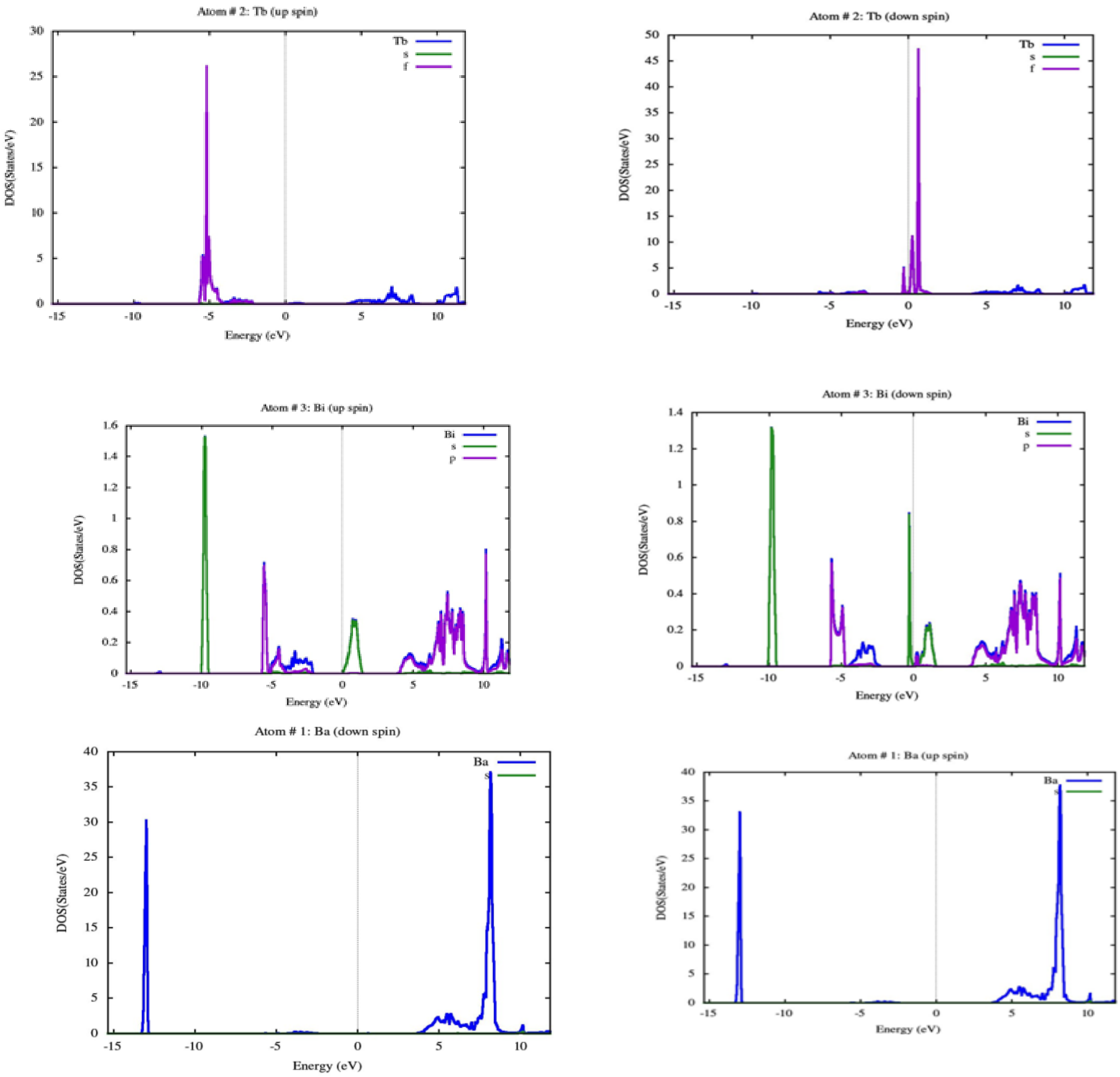

Figure III.7. Density of states for spin (up) and spin (dn) configuration of (a) Ba_2SmBiO_6 (b) Ba_2TbBiO_6 using mBJ-GGA

III.6 Optical properties

III.6.1 Dielectric Function ε(ω)

This property represents the electronic response of solid materials to electromagnetic radiation. The dielectric function is mathematically expressed as follows:

$$\varepsilon(\omega) = \varepsilon_1(\omega) + i\varepsilon_2(\omega) \qquad \text{(III.4.1)}$$

Where:

ε(ω): is the complex dielectric function.

$\varepsilon_1(\omega)$: the real part, which characterizes the dispersion of light within the material.

$\varepsilon_2(\omega)$: the imaginary part, which characterizes the absorption of light by the material.

By knowing both the real and imaginary parts of the dielectric function, it becomes possible to determine other optical constants such as the refractive index n(ω), the absorption coefficient α(ω), among others

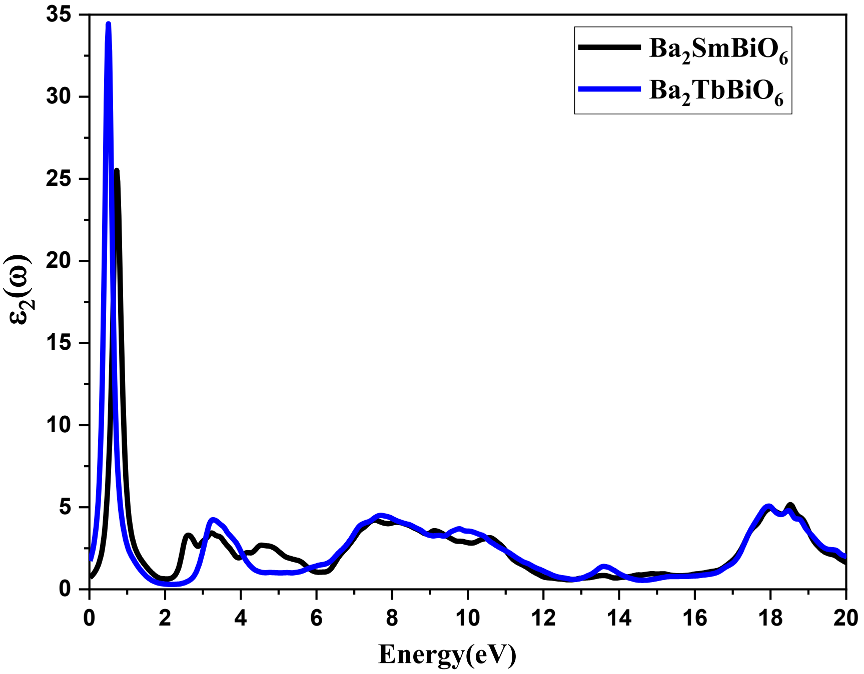

Figure III.8. Imaginary part of the dielectric function (ε_2) as a function of energy for Ba_2SmBiO_6 and Ba_2TbBiO_6

The spectral analysis of the imaginary dielectric function $\varepsilon_2(\omega)$ reveals the following key observations:

- **Low-Energy Region (0–2 eV):**

A sharp peak is observed around 0.5 eV in both compounds, indicating strong interband electronic transitions. Ba_2TbBiO_6 exhibits a higher peak value (34.46) compared to Ba_2SmBiO_6 (25.43), suggesting a stronger optical response in the low-energy region for the terbium-based compound.

- **Mid-Energy Region (2–12 eV):**

This region is characterized by several smaller peaks corresponding to secondary electronic transitions between energy levels. Although both compounds show similar general behavior, slight differences in the intensity and position of these peaks are noted, which may be attributed to the differing electronic effects of the rare-earth elements (Sm vs. Tb).

- **High-Energy Region (>16 eV):**

A distinct peak is evident in the $\varepsilon_2(\omega)$ spectrum of Ba_2TbBiO_6, which is not clearly observed in Ba_2SmBiO_6. This may be associated with higher-energy electronic transitions or optical phenomena such as plasmon resonance interactions with higher energy bands.

The analysis demonstrates that Ba_2TbBiO_6 exhibits stronger optical activity than Ba_2SmBiO_6, particularly in the low-energy region. These findings support its potential for advanced optical applications, including photodetectors, light-tuning lenses, and photovoltaic components.

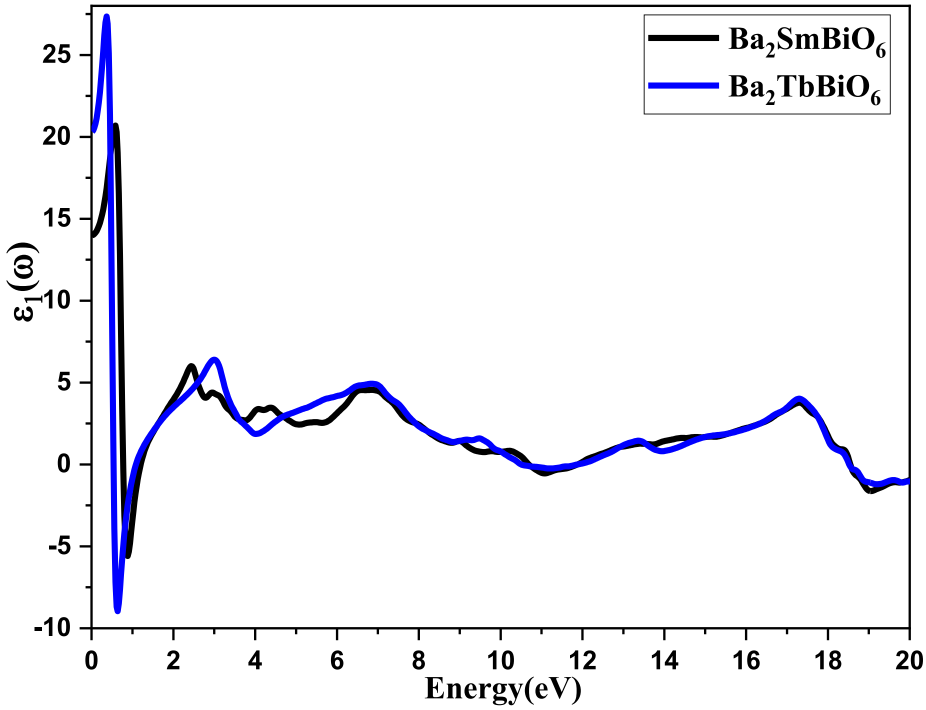

Figure III.9. Real part of the dielectric function analysis for Ba_2SmBiO_6 and Ba_2TbBiO_6 compounds

- **Low-Energy Region (0–2 eV):**

A sharp peak is observed for both compounds at low photon energies, where Ba_2TbBiO_6 exhibits a maximum value of around 27.32, while Ba_2SmBiO_6 reaches approximately 20,49. This strong positive $\varepsilon_1(\omega)$ value indicates significant polarizability and strong interaction with incident radiation. A notable dip into negative values is also seen around 1 eV, particularly for Ba_2TbBiO_6, suggesting a potential for metallic-like behavior or plasma oscillation characteristics in this narrow energy range.

- **Intermediate Region (2–12 eV):**

Multiple oscillations are present in both curves, indicating complex interband transitions. These features are associated with the contributions of different electronic states to the dielectric response, with Ba_2TbBiO_6 generally displaying slightly higher $\varepsilon_1(\omega)$ values than Ba_2SmBiO_6, suggesting enhanced dispersion characteristics.

- **High-Energy Region (12–20 eV):**

In this region, $\varepsilon_1(\omega)$ for both compounds stabilizes around small positive values, with Ba_2TbBiO_6 showing a slightly more pronounced peak near 17 eV. This behavior may be attributed to high-energy interband transitions or saturation in the dielectric response due to limited electronic contributions at higher photon energies.

The comparative analysis of the real dielectric function reveals that Ba_2TbBiO_6 possesses a slightly stronger dielectric response than Ba_2SmBiO_6 across the energy range studied. The presence of a negative $\varepsilon_1(\omega)$ region and stronger peaks at low energy suggest that Ba_2TbBiO_6 may offer better performance in applications involving high refractive index or plasmonic behavior. These findings support its potential use in advanced optical and energy-related devices.

III.6.2 Refractive Index :

The refractive index is defined as the ratio between the speed of light in vacuum (C) and its speed in the medium (v), (n=c/v) ,and it is the real part of the complex refractive index n(ω) .

$$N(\omega) = n(\omega) + ik(\omega) \qquad \textbf{(III.4.2)}$$

n(ω):*The real part of the complex refractive index (refractive index), given by the relation:*

$$n(\omega) = \left(\left[\{\varepsilon^2 1(\omega) + \varepsilon^2 2(\omega)\}\frac{1}{2} + \varepsilon 1\ (\omega)\right]\frac{1}{2}\right)/\sqrt{2} \qquad \textbf{(III.4.3)}$$

- **Low-Energy Region (0–2 eV)**

Both compounds show a sharp rise in the refractive index at low energies, reaching peak values above 5. This indicates strong light-matter interaction and suggests the presence of low-energy electronic transitions, possibly associated with narrow bandgaps. The slightly higher refractive index for Ba_2TbBiO_6 in this region may point to a more polarizable electronic structure due to the presence of Tb.

- **Intermediate Region (2–10 eV)**

In this range, the refractive index exhibits a series of oscillations, with multiple peaks and dips. These features are attributed to interband transitions involving Bi-6p, O-2p, and rare-earth f orbitals. The two materials exhibit similar overall trends, with minor shifts in peak positions and magnitudes. Such differences highlight the role of the rare-earth substitution in tuning the electronic structure and optical transitions.

- **High-Energy Region (10–20 eV)**

At higher energies, the refractive index generally decreases and flattens, although small fluctuations remain. This behavior reflects the reduced optical response due to the fewer available states at high energies and the dominance of core-level transitions. Ba_2TbBiO_6 continues to show a slightly higher refractive index, suggesting it retains stronger polarization effects across the entire energy range.

The refractive index dispersion curves of Ba_2SmBiO_6 and Ba_2TbBiO_6 reveal strong low-energy optical activity and a sensitive dependence on the choice of rare-earth ion. The materials exhibit properties favorable for photonic applications, and their optical behavior can be fine-tuned via compositional substitution. Future studies involving experimental validation and further theoretical modeling are recommended to explore practical device integration.

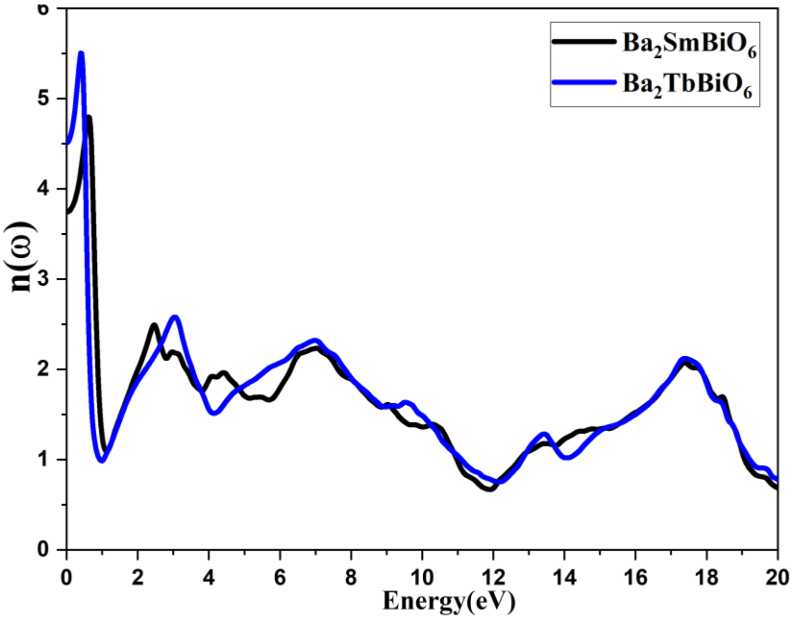

Figure III.10. The variations of the real part of the refractive index with photon energy for Ba_2SmBiO_6 and Ba_2TbBiO_6

III.6.3 The Extinction Coefficient

It is the imaginary part of the complex refractive index and expresses the amount of energy absorbed by the material's electrons from the energy of incident photons, and it is given by the following relation:

$$\boldsymbol{k(\omega) = \left(\left[\{\varepsilon^2 1(\omega) + \varepsilon^2 2(\omega)\}\frac{1}{2} + \varepsilon 1\,(\omega)\right]\frac{1}{2}\right)/\sqrt{2}} \qquad (\mathbf{III.4.4})$$

Where, we note:

- **Low-Energy Region (0–2 eV):**

A sharp and intense peak is observed for both compounds, with Ba_2SmBiO_6 showing a slightly higher magnitude. This indicates stronger light absorption at low photon energies, possibly linked to narrow bandgap transitions.

- **Mid-Energy Region (2–10 eV):**

The absorption behavior diverges between the two materials. Ba_2TbBiO_6 exhibits more pronounced peaks in the 6–10 eV range, suggesting enhanced optical transitions, likely due to crystal field effects or hybridization involving Tb 4f states.

- **High-Energy Region (10–20 eV):**

Both materials display similar trends with broad absorption features. Peaks around 18 eV indicate transitions from deeper valence states to the conduction band.

The overall trend suggests that the substitution of Sm with Tb leads to an increase in absorption intensity in the mid-energy region while slightly reducing absorption at low energies. These variations highlight the influence of rare-earth ions on the electronic structure and optical response.

Ba_2SmBiO_6 and Ba_2TbBiO_6 exhibit comparable yet distinguishable optical behaviors, with significant differences in their extinction coefficients at specific energy ranges. The findings demonstrate that rare-earth ion substitution can effectively tune the optical properties of double perovskites, providing a pathway for material optimization in photonic and optoelectronic applications.

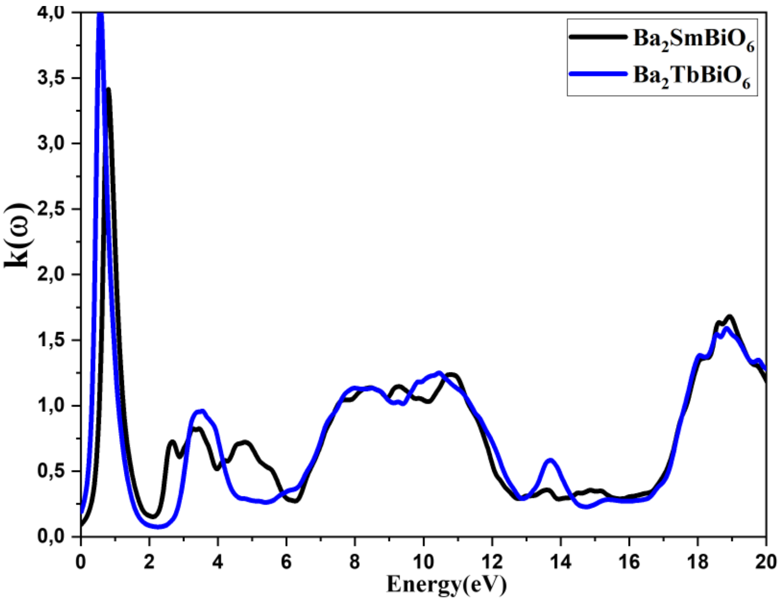

Figure III.11. Variation of the extinction coefficient with photon energy for Ba_2SmBiO_6 and Ba_2TbBiO_6 compounds

III.6.4 Absorption Coefficient: α(ω)

It is a measure of the ability of a material to absorb light or electromagnetic radiation as it passes through it. The absorption coefficient can be related to the dielectric function by the following relation:

$$\alpha(\omega) = \frac{\varepsilon^{2(\omega)}.\omega}{c.n} \quad \textbf{(III.4.5)}$$

Where:

ω: is the angular frequency

c; is the speed of light in vacuum

n; is the refractive index

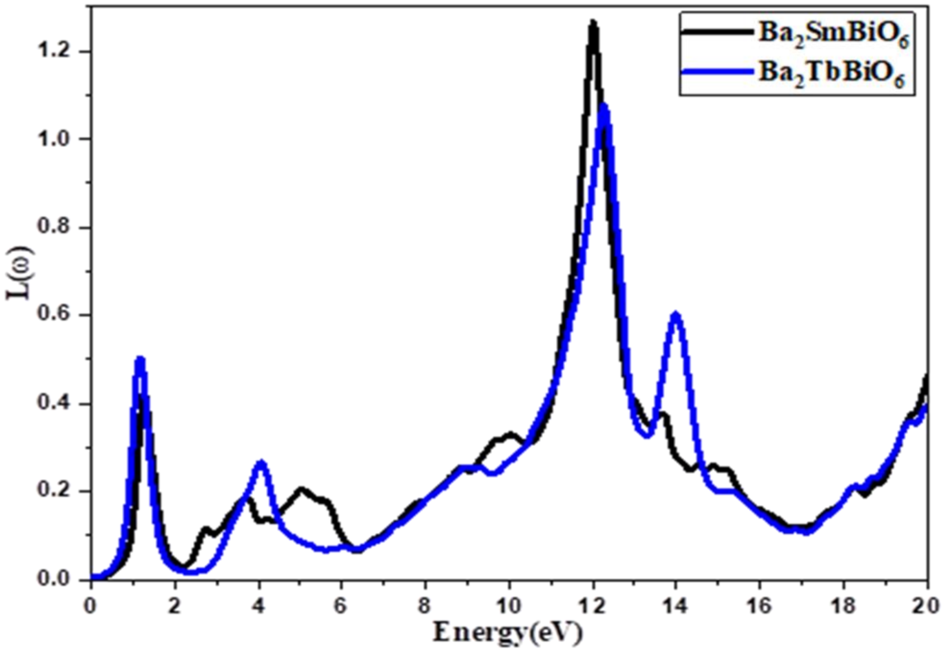

Figure III.12.The absorption coefficients of the compound Ba_2BBiO_6 (B= Sm, Tb) using the GGA approximation

The absorption coefficient (α(ω)) curve for both compounds, Ba_2SmBiO_6 and Ba_2TbBiO_6, shows a similar optical behavior, indicating a strong ability to absorb light in both the visible and ultraviolet (UV) regions. Absorption begins significantly after exceeding the band gap energy, where a sharp increase in the absorption coefficient is observed. This rise reflects direct electronic transitions from the valence band to the conduction band.

A main peak in the absorption coefficient appears at around 3.0 eV for both materials, suggesting high efficiency in absorbing visible light. Moreover, the curve continues to show strong absorption in the UV region, which indicates electronic transitions from deeper energy levels or within the band itself.

This optical behavior makes Ba_2SmBiO_6 and Ba_2TbBiO_6 promising candidates for optoelectronic applications, such as solar cells and UV photodetectors, due to their high light absorption capability and efficient light–matter interaction.

III.6.5 The energy loss function (L(ω))

It is an important factor for describing the energy loss of a fast electron passing through a material, and its basic expression is written as**:**

$$\mathbf{L}(\boldsymbol{\omega})\left|=\frac{\varepsilon_2(\omega)}{\varepsilon_1{}^2(\omega)+\varepsilon_2{}^2(\omega)}\right| \qquad \textbf{(III.4.6)}$$

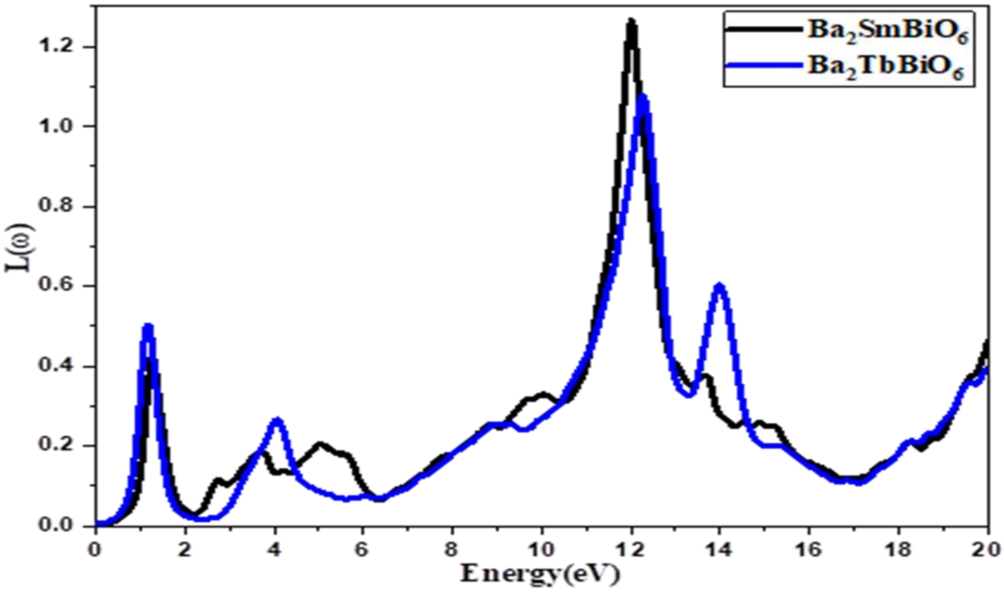

Figure III.13.The energy loss function for Ba_2BBiO_6 (B= Sm, Tb) perovskites utilising mBJ-GGA.

The energy loss function (L(ω)) for both Ba_2SmBiO_6 and Ba_2TbBiO_6 shows a similar pattern, which means both materials lose energy effectively when they interact with light in the visible and ultraviolet (UV) regions. The main peak in the energy loss appears at 10 eV for both materials, showing that strong electronic transitions are happening between the valence band and the conduction band.

This behavior matches the nature of each material: Ba_2SmBiO_6 acts like a spin-dependent half-metal, while Ba_2TbBiO_6 behaves as a direct band gap semiconductor with a gap of 1.79 eV. A smaller second peak appears at higher energies (18–20 eV), which may come from deeper electronic transitions related to Tb-f and Bi-d or Bi-p orbitals.

III.6.6 Optical Conductivity σ(ω)

Optical conductivity refers to a material's ability to interact with light or electromagnetic radiation in the optical spectrum. It describes the material's capacity to absorb or transmit optical energy when exposed to light. It is expressed by the relation :

$$\sigma(\omega) = \frac{\alpha n c}{4\pi} \qquad \textbf{(III.4.6)}$$

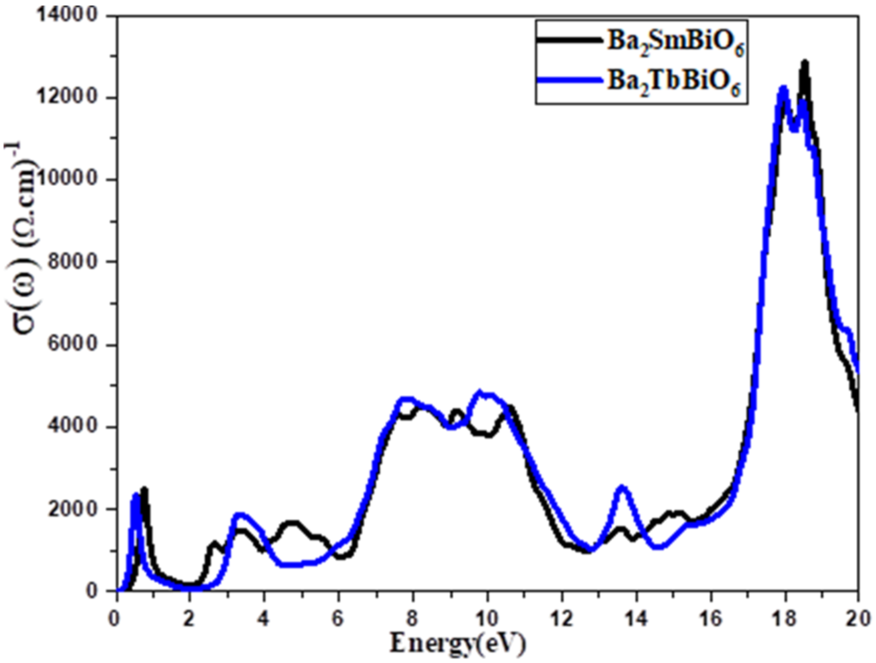

Figure III.14.Optical conductivity curve (σ(ω)) for both compounds, Ba_2SmBiO_6 and Ba_2TbBiO_6

The optical conductivity curve (σ(ω)) for both compounds, Ba_2SmBiO_6 and Ba_2TbBiO_6, shows a similar trend, indicating strong conductivity when interacting with light in the visible and ultraviolet (UV) regions. Conductivity begins to increase significantly after crossing the band gap (~1.79 eV), which is a sign of direct electronic transitions from the valence band to the conduction band. This makes both materials promising candidates for optical and optoelectronic applications.

The main peak of the conductivity appears at 10 eV for both materials, suggesting a high efficiency in converting light energy into electrical energy. This result is consistent with the band structure analysis, which shows that Ba_2SmBiO_6 has spin-dependent half-metallic behavior, while Ba_2TbBiO_6 behaves as a direct band gap semiconductor with a fixed gap of 1.79 eV, independent of spin channels. These differences in electronic band structures are clearly reflected in the shape of the σ(ω) curve, especially in terms of peak distribution and its connection to electronic transitions from deep levels or within the bands.

Detailed analysis confirms that the main orbitals involved in these transitions are Sm-d, Tb-f, Bi-p, and O-p. Sm-d and Bi-p orbitals contribute strongly to the conduction band (CB), while O-p and Tb-f orbitals are present in both the valence and conduction bands. This orbital distribution enhances the interaction between electrons and photons, leading to higher conductivity values in the relevant energy ranges.

In addition, a secondary increase in conductivity is observed at higher photon energies (~18–20 eV), which can be attributed to ultraviolet transitions or transitions from deep energy levels within the bands, mainly associated with Tb-f and Bi-d orbitals. This supports the use of these materials in applications that require strong interaction with UV radiation, such as UV detectors or UV-protective materials.

Based on these theoretical results, which are in good agreement with the structural and optical properties discussed in the paper, it can be concluded that both compounds possess excellent electronic conductivity features. This makes them suitable candidates for use in solar cells, light detection devices, and spintronic technologies — especially Ba_2SmBiO_6, which shows a distinct half-metallic behavior.

Table III.4. Comparison Between Ba_2SmBiO_6 and Ba_2TbBiO_6

Property	**Ba_2SmBiO_6 (Half-Metallic)**	**Ba_2TbBiO_6 (Direct Band Gap Semiconductor)**
Type of Material	Half-metallic	Semiconductor (Direct Band Gap)
Band Gap	~1.79 eV (spin down)	~1.78 eV (all spins)
Nature of Band Gap	Spin-dependent	No spin dependence
Absorption Coefficient α(ω)	UV absorption in the spin-down channel	UV absorption in all spin channels
Absorption Edge	~1.8 eV (in the spin-down channel)	~1.78 eV (same for all spins)

Real Part of Dielectric Function	At low energy ~2.02	~2.02
Refractive Index	UV region	UV region
Reflectivity	UV region	UV region
Use in Spintronics	Yes (Spin Filters, Magnetic Tunnel Junctions)	No (because it's not spin-dependent)
Use in Solar Cells	No (UV absorption is not enough)	Yes (UV absorption is good)
Use in Photodetectors	Yes (UV detectors)	Yes (UV detectors)
Use in LEDs	No (not suitable)	Yes (UV emission possible)
Use in Optical Devices	No (does not exhibit absorption/emission in visible range)	Yes (absorption/emission in UV)

III.7 Conclusion

Based on the results obtained from the theoretical investigation of the Ba_2SmBiO_6 and Ba_2TbBiO_6 compounds using DFT methodology with precise techniques such as the FP-LAPW method and the mBJ-GGA functional, it can be concluded that each compound exhibits distinct electronic and optical properties that qualify them for advanced technological applications. The Ba_2SmBiO_6 compound demonstrated spin-dependent half-metallic behavior, which opens up promising prospects for its use in spintronic applications, where electron spin is exploited for more efficient information storage and processing. On the other hand, Ba_2TbBiO_6 exhibited characteristics of a direct bandgap semiconductor, making it suitable for energy and optoelectronic applications such as solar cells and photodetectors.

These findings highlight the importance of exploring double perovskite compounds as promising platforms for modern technological fields and emphasize the role of accurate theoretical design in predicting material properties prior to synthesis. Therefore, this study represents a significant step toward the development of new functional materials that can enhance the performance of future electronic and optical devices.

[1]- Yanju Wang, Lingkong Zhang, Shuailing Ma, «Octahedral tilting dominated phase transition in compressed double perovskite Ba2SmBiO6» ,Appl. Phys. Lett. 118,2021 .

[2] P. Blaha, K. Schwarz, G. Madsen, D. Kvasnicka, J. Luitz, Wien2k, Techn. Universitat, Vienna, Austria, (2001).

[3] J. P. Perdew, K. Burke, M. Ernzerhof, Phys. Rev. Lett. 77 (1996) 3865.

[4] J.P. Perdew, Y. Wang, Phys. Rev. B 45 (1992) 13244-13249.

[5] F. D. Murnaghan, Proc. Nat. Acad. Sci.USA 30 (1944) 244.

[6] Anon Exploring Novel Ba2MBiO6 (M = Sm, Tb) Oxide Double Perovskites Employing DFT | Journal of Inorganic and Organometallic Polymers and Materials.

[7] Anon Exploring Silicon-Based Ca2TiSiO6 Ordered Double Perovskite Oxides: a Comprehensive DFT Investigation of Structural, Dynamical, Mechanical Stability, and Optoelectronic Properties | Silicon .

General Conclusion

This study provided an in-depth understanding of the electronic and optical properties of the double perovskite compounds Ba_2SmBiO_6 and Ba_2TbBiO_6 using density functional theory (DFT) supported by advanced computational techniques. The results revealed that Ba_2SmBiO_6 exhibits spin-dependent half-metallic behavior, making it highly suitable for spintronic applications. On the other hand, Ba_2TbBiO_6 demonstrated direct bandgap semiconductor characteristics, positioning it as a promising candidate for solar energy and photodetection applications.

These findings highlight the significant potential of Ba_2BBiO_6-type double perovskite compounds in the development of future high-efficiency, low-cost electronic and optoelectronic devices. Moreover, they open new avenues for designing multifunctional materials that combine both magnetic and optical properties, thus broadening the scope of materials used in advanced technologies such as spintronics and photovoltaic systems.

Abstract

This study focuses on the investigation of the electronic and optical properties of the double perovskite compound Ba_2BBiO_6, where the B-site is occupied by either samarium or terbium, employing advanced computational methods within the framework of Density Functional Theory (DFT). The findings reveal that Ba_2SmBiO_6 exhibits spin-dependent half-metallic behavior, indicating its suitability for spintronic applications, whereas Ba_2TbBiO_6 demonstrates direct bandgap semiconducting behavior, making it a promising material for solar energy harvesting and photodetection. These results underscore the potential of these compounds in the development of high-efficiency, cost-effective photovoltaic devices.

Keywords : Double perovskite, Density Functional Theory (DFT), Electronic properties, Optical properties, Half-metal, Spintronics, Bandgap, Solar cells, Complex oxides.

Résumé

Cette étude porte sur l’analyse des propriétés électroniques et optiques du composé à double pérovskite Ba_2BBiO_6, dans lequel le site B est occupé soit par le samarium, soit par le terbium, en recourant à des méthodes de calcul avancées basées sur la théorie de la fonctionnelle de la densité (DFT). Les résultats montrent que le Ba_2SmBiO_6 présente un comportement demi-métallique dépendant du spin, ce qui le rend adapté aux applications en spintronique, tandis que le Ba_2TbBiO_6 se comporte comme un semi-conducteur à gap direct, le rendant prometteur pour des applications dans le domaine de l’énergie solaire et de la photodétection. Ces conclusions mettent en évidence le potentiel de ces matériaux pour le développement de dispositifs photovoltaïques à haut rendement et faible coût.

Mots clés : Double pérovskite, Théorie de la fonctionnelle de la densité (DFT), Propriétés électroniques, Propriétés optiques, Demi-métal, Spintronique, Bande interdite, Cellules solaires, Oxydes complexes.

ملخص

يتناول البحث دراسة الخصائص الإلكترونية والبصرية لمركب البيروفيسكايت المزدوج Ba_2BBiO_6، حيث يكون العنصر B إما الساماريوم أو التيربيوم، باستخدام تقنيات حسابية متقدمة ضمن نظرية الكثافة الوظيفية (DFT). أظهرت النتائج أن Ba_2SmBiO_6 يمتلك خصائص نصف فلزية تعتمد على اللف المغزلي، مما يجعله مناسبًا لتطبيقات الإلكترونيات المغزلية، في حين أن Ba_2TbBiO_6 يُظهر سلوك شبه موصل مباشر الفجوة، مما يؤهله لتطبيقات الطاقة الشمسية والكشف الضوئي. تشير هذه النتائج إلى إمكانية استخدام هذه المركبات في تطوير أجهزة كهروضوئية عالية الكفاءة ومنخفضة التكلفة .

الكلمات الرئيسية: البيروفسكايت المزدوج، نظرية الكثافة الوظيفية (DFT)، الخصائص الإلكترونية، الخصائص البصرية، نصف معدن، الإلكترونيات المغزلية، فجوة النطاق، الخلايا الشمسية، الأكاسيد المعقدة.